FACULDADE DE ENGENHARIA DA UNIVERSIDADE DO PORTO

Airborne Wind Energy Systems: Modelling, Simulation and Economic Analysis

Manuel Côrte-Real de Matos Fernandes

Mestrado Integrado em Engenharia Electrotécnica e Computadores

Supervisor: Fernando A.C.C. Fontes

Second Supervisor: Luís Tiago Paiva

August 2, 2018

Airborne Wind Energy Systems: Modelling, Simulation and Economic Analysis

Manuel Côrte-Real de Matos Fernandes

Mestrado Integrado em Engenharia Electrotécnica e Computadores

August 2, 2018

Resumo

Nesta dissertação, é abordado o problema de produção de energia elétrica utilizando um Airborne Wind Energy System, especificamente um Pumping Kite Generator. O sistema é constituído por uma asa presa a um cabo que a liga a um gerador elétrico através de um tambor, produzindo energia elétrica através da tensão no cabo enquanto a asa se move numa trajetória aproximadamente ortogonal à direção do vento. Quando o comprimento máximo do cabo é atingido, a asa é controlada de forma a minimizar a tensão no cabo e é recolhida até uma posição inicial da qual reinicia o ciclo de produção.

Baseado mo modelo dinâmico da asa, um modelo de Matlab/Simulink é desenvolvido e usado para simular e analisar o movimento de uma asa subaquática vista de cima e de um Pumping Kite Generator numa perspetiva 2D vista de lado e de uma perspetiva 3D. É desenvolvido um controlador de trajetória que permite o movimento da asa num caminho prédefinido de forma a maximizar a produção de energia elétrica e uma estratégia de manobra para rajadas de vento de forma a evitar forças de tensão excessivas no cabo. Através de uma seleção empírica de parâmetros de controlo, é construída a curva de potência do sistema definido e são desenvolvidos estudos económicos baseados nas características de vento estimadas para um determinado local.

É ainda abordada a questão do uso da área do solo de um parque eólico de Pumping Kite Generators, analisando o espaçamento mínimo entre unidades e uma possibilidade de sincronização das diferentes unidades para uma produção regular, evitando as variações periódicas inerentes a sistemas deste género.

Abstract

In this dissertation, we address the problem of electrical energy generation with an Airborne Wind Energy System, specifically a Pumping Kite Generator. The system is constituted by a tethered kite attached to an electric generator through a winch drum and it produces electricity through the traction force on the tether while the kite moves in an approximately crosswind motion. When a maximum tether length is reached, the kite is controlled to minimize the tether tension and it is retrieved to an initial position to restart the production cycle.

Based on a dynamic model of the kite, a Matlab/Simulink model is developed and used to simulate and analyze the motion of an underwater kite in a top-view perspective and the motion of a Pumping Kite Generator in a 2D side-view and 3D perspective. It is developed a trajectory controller that allows the kite to move in a defined path in order to maximize the power production and a wind gust handling strategy to avoid overwhelming tether tension forces. Through an empirical selection of control parameters, we construct the power curve of the defined system and we develop further economical studies based on wind characteristics estimations for a given site.

We approach the problem of ground area usage in a kite wind farm, assessing the minimum spacing between units and possible synchronization settings for a steady total electrical output, avoiding the inherent periodic variations of such a system.

Acknowledgments

I would like to thank my supervisors Fernando Fontes and Luís Tiago Paiva for all the help and for giving me the possibility to work in such an interesting topic. I would also like to thank my colleague Gonçalo Silva for the comradeship during the past six months.

I would like to thank my family for all the support they gave me and my colleagues and friends who have showed me that companionship and cooperation are the best tools to thrive.

Finally, I thank the support of the projects PTDC-EEI-AUT-2933–2014j16858–TOCCATA and 02/SAICT/2017–31447-FCT–UPWIND - funded by FEDER funds through COMPETE2020 - Programa Operacional Competitividade e Internacionalização (POCI) and by national funds (PIDDAC) through FCT/MCTES.

Manuel Fernandes

"A kite is a victim you are sure of.
You love it because it pulls
gentle enough to call you master,
strong enough to call you fool;"

Leonard Cohen ("A Kite is a victim", 1965)

Contents

1 Introduction **1**

2 Airborne Wind Energy Systems **3**
2.1 GG-AWES . . . 3
2.2 FG-AWES . . . 4
2.3 AWES Under Development . . . 4
2.3.1 GG-AWES Under Development . . . 4
2.3.2 FG-AWES Under Development . . . 7

3 Dynamic Model of the Kite Power System **9**
3.1 Coordinate System . . . 9
3.2 Acting Forces . . . 11
3.3 Dynamic Model . . . 13

4 Kite Power System Simulation **15**
4.1 Underwater Kite . . . 15
4.2 Elevation variation with the Angle of Attack and Wind Speed . . . 16
4.3 2D Simulation . . . 20
4.4 3D Simulation . . . 20
4.4.1 Trajectory Controller and Wind Gusts Response . . . 21
4.4.2 Simulation Results . . . 22

5 Local Wind Characteristics and Power Curve Construction **29**
5.1 Wind Resource Characterization . . . 29
5.1.1 Power Spectral Density . . . 29
5.1.2 Speed and Power Relations . . . 31
5.1.3 Weibull and Rayleigh Distribution . . . 31
5.2 Local Characterization . . . 31
5.2.1 Global Wind Atlas . . . 31
5.2.2 Local Characterization . . . 32
5.3 Empirical Selection of Parameters for Maximization of Energy Output . . . 35
5.4 Power Curve, Average Power and Capacity Factor . . . 36

6 Economical Analysis **41**
6.1 Efficiency and Annual Energy Production (AEP) . . . 41
6.2 Initial Capital Cost (ICC) . . . 41
6.2.1 Aircraft and Tether . . . 42
6.2.2 Electric Power Generation and Interface Components . . . 42
6.2.3 Other Components . . . 42

6.3 Operation and Maintenance (O&M) and Replacement Costs 43
6.4 Levelized Cost of Energy (LCOE) 44

7 Wind Farm Ground Area Usage **45**
7.1 Spacing of KPS Units 45
7.2 Electrical Output 47

8 Conclusions and Future Work **51**

A Auxiliary Equations **53**
A.1 2D Model 53
A.2 3D Model 54

B 3D Matlab/Simulink Model Subsystems **57**

List of Figures

1.1 Carbon Dioxide Concentrations in the Atmosphere. 2

2.1 Institutions With Airborne Wind Energy Projects. 5
2.2 e-Kite e100 System. 5
2.3 Enerkite ek30, 30kW System. 6
2.4 KiteGen Carousel. 6
2.5 Altaeros Buoyant Airborne Turbine. 7

3.1 Global and Local Coordinate Systems. 10
3.2 Body Coordinate System. 10
3.3 Roll Angle Variation for a Two Line Kite. 11
3.4 Angle of Attack. 12
3.5 Acting Forces. 13

4.1 Underwater Kite Simulink Model. 17
4.2 Underwater Kite Trajectory. 17
4.3 Underwater Kite State Variables (r,ϕ) and Control Variable (ψ). 17
4.4 Variation of β for α Equal to $0^o, 5^o$ and 10^o. 19
4.5 Variation of β for α Equal to 12^o and 13^o. 19
4.6 Complete Cycle for 2D Simulation. 20
4.7 2D Simulation State Variables (r,β) and Control Variable (α). 21
4.8 2D Matlab/Simulink Model. 22
4.9 3D Simulink Model. 23
4.10 Trajectory Controller Schematic Figure. 23
4.11 Follow Path with Constant Tether Length and Wind Gust Response. 23
4.12 Follow Path with Full Production Cycle and Wind Gust Response. 24
4.13 Tether Force with Fixed Tether Length and Without Wind Gust Response in a 100s Simulation. 24
4.14 Tether Force with Fixed Tether Length and Wind Gust Response in a 100s Simulation. 25
4.15 State Variables (r,ϕ,β) for a Complete Production Cycle with Wind Gust Response. 25
4.16 Complete Production Cycle Trajectory of a 2000s Simulation with $v_w = 10m/s$. . 26
4.17 State variables (β,ϕ) of a 2000s Simulation With $v_w = 10m/s$. 27
4.18 Power (W) and Energy (J) Output of a 2000s Simulation with $v_w = 10m/s$. 27

5.1 Typical Power Spectral Density. 30
5.2 Global Wind Atlas Method. 32
5.3 Praia do Cabedelo Characteristics. 33
5.4 Predominant Wind Direction For Praia do Cabedelo. 33

5.5 Gamma Function - $\Gamma\left(1+\frac{1}{k}\right)$. 34
5.6 Rayleigh Probability Density Function For Praia do Cabedelo For Altitudes Of $50, 100$ and $200m$. 34
5.7 Mechanical Power Output. 35
5.8 Complete Production Cycle Of A 2000s Simulation With $v_w = 7m/s$. 36
5.9 State Variables (β, ϕ) Of A 2000s Simulation In Degrees With $v_w = 7m/s$. 37
5.10 Mechanical Power Output. 38
5.11 Power Curve. 38
5.12 Power Curves For 1, 1.5 And 2kW Average Power Output limits. 39

7.1 Minimum Distance Between Parallel Kites. 46
7.2 Minimum Distance Between Aligned Kites. 46
7.3 Kites Orientation And Phase Shifts. 48
7.4 Overlapped Trajectories Of Different Phase Shifts. 48
7.5 Energy Production Of A Single KPS Unit And A 4x4 Wind Farm. 49
7.6 LCOE Variation With The Number Of Units In A Wind Farm. 49

B.1 3D Matlab/Simulink Model. 58
B.2 Centrifugal Force Subsystem. 59
B.3 Coriolis Force Subsystem. 60
B.4 Force of Gravity Subsystem. 61
B.5 Aerodynamic Forces Subsystem. 62
B.6 $\ddot{\mathbf{p}}$ Subsystem. 63
B.7 $\ddot{\phi}$ Subsystem. 64
B.8 $\ddot{\beta}$ Subsystem. 65
B.9 Wind Apparent Velocity Subsystem. 66

List of Tables

4.1 Underwater Kite Simulation Parameters 16
4.2 2D Simulation Parameters 18
4.3 Natural Elevation Angle 18
4.4 Simulation Parameters and Conditions 26

5.1 Annual Average Wind Speeds and Scale Parameters for Altitudes of $50, 100$ and $200m$ 32
5.2 Parameters for Energy Output Maximization 40

6.1 Cost Breakdown of System Components 43
6.2 LCOE Forecasts 44

Abbreviations and Symbols

AWES	Airborne Wind Energy Systems
KPS	Kite Power Systems
PKG	Pumping Kite Generator
LCOE	Levelized Cost of Energy
FG	Flying Generation
GG	Ground Generation
PSD	Power Spectral Density
GWA	Global Wind Atlas
A	wing reference area of kite $\left[\mathrm{m}^2\right]$
R_{GL}	rotation matrix from G to L
$\mathit{Æ}$	wing aspect ratio
R_{LG}	rotation matrix from L to G
a_t	tether reel–out acceleration $\left[\mathrm{m\,s}^{-2}\right]$
r	tether length [m]
c_{D}	aerodynamic drag coefficient
ρ	air density $\left[\mathrm{kg\,m}^{-3}\right]$
c_{L}	aerodynamic lift coefficient
s	wing span [m]
E	energy produced [Ws]
T	tether tension [N]
$\vec{\mathrm{F}}^{\mathrm{aer}}$	aerodynamic force [N]
$\mathbf{v}_a$	apparent wind velocity $\left[\mathrm{m\,s}^{-1}\right]$
$\vec{\mathrm{F}}^{\mathrm{drag}}$	drag force [N]
$\mathbf{v}_w$	wind velocity $\left[\mathrm{m\,s}^{-1}\right]$
$\vec{\mathrm{F}}^{\mathrm{cent}}$	centrifugal force [N]
v_t	tether reel–out velocity $\left[\mathrm{m\,s}^{-1}\right]$
$\vec{\mathrm{F}}^{\mathrm{cor}}$	Coriolis force [N]
$\vec{\mathrm{F}}^{\mathrm{lift}}$	aerodynamic lift force [N]
$\mathbf{u}$	control vector
$\vec{\mathrm{F}}^{\mathrm{inert}}$	inertial forces [N]
$\mathbf{x}$	state vector
$\vec{\mathrm{F}}^{\mathrm{th}}$	tether force [N]
α	angle of attack [rad]
g	gravitational acceleration $\left[\mathrm{m\,s}^{-2}\right]$
ϕ	azimuthal angle [rad]
m	mass [kg]
β	elevation angle [rad]
P	power produced [W]
θ	polar angle [rad]
R_{90}	90° anticlockwise rotation matrix
ψ	roll angle [rad]

Preface

This dissertation is part of the UPWind Project [1], which aims to explore Airborne Wind Energy Systems. The project focuses on systems based on a tethered wing flying at a high speed crosswind motion and focuses on three questions:

- Identification, Modelling and Estimation of AWES
- Optimization and Control of AWES
- Multiple Kite Systems

An article regarding the trajectory controller and wind gust handling method described in Subsection 4.4.1 is to appear in 15th International Conference on Informatics in Control, Automation and Robotics (ICINCO) [2].

Chapter 1

Introduction

The current dependence on fossil fuels and non-renewable resources for our economic activities has led to a precarious and dangerous paradigm with uncountable environmental and social consequences.

In 2017 a record breaking value of $410ppm$ of carbon dioxide concentration in the atmosphere was reached, strengthening the greenhouse effect and accelerating climate change [3]. In an effort to reduce fossil fuel dependency, the European Union has set targets for the decrease of 20% of greenhouse gas emissions (compared with 1990 levels) and the increase in 20% of the energy derived from renewable sources and energy efficiency in the EU for the year 2020 [4].

In order to achieve a sustainable lifestyle, several renewable sources of energy have been explored throughout the last decades with increasing dissemination and efficiency.

Renewable energy sources "represented almost two-thirds of new net electricity capacity additions in 2016, with almost 165 gigawatts (GW) coming online" [5]. One of these has been the conversion of the wind kinetic energy into electric energy using wind turbines which has reached, in 2017, a global capacity of 539GW [6].

The wind velocity is stronger and more stable at higher altitudes, which means that, although the air is less dense, the kinetic power will be larger as well. This has caused an increase of wind turbines heights throughout the years, allowing larger power outputs and generally higher capacity factors.

However, higher towers require more materials and cause larger expenditures, making this altitude quest economically and logistically unfeasible above certain limits. Following the Square-Cube Law, the energy output grows with the swept area as a function of the blades length square, but structure volume and mass and consequently the cost grows with the cube of the radius [7].

To surpass this obstacle, different kinds of Airborne Wind Energy Systems (AWES) are being developed, permitting the exploration of higher winds with a light infrastructure.

One of the most promising systems is the Pumping Kite Generator (PKG), which is based on a tethered airfoil connected to an electrical generator through a winch drum. This system produces electric energy when the tether is being reeled-out and consumes a fraction of the generated electricity to reel back in the tether, restarting the cycle.

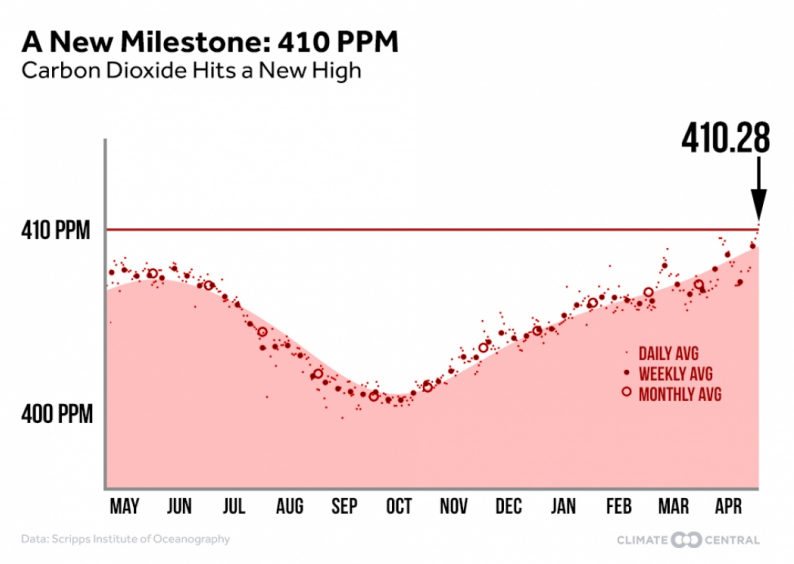

Figure 1.1: Carbon Dioxide Concentrations in the Atmosphere [3].

This dissertation parts from a dynamic model of a PKG system, described in Chapter 3, to develop Matlab/Simulink models that simulate the kite motion and behaviour. Chapter 4 outlines the Matlab/Simulink models for an underwater kite, a 2D and a 3D perspective of a PKG system and displays the respective simulation results. In Section 5.3, through empirical selection of control parameters, we estimate the possible mechanical power output of the system which is used with the wind model characterization, developed in Chapter 5, to determine the system power curve, average annual power output and capacity factor in Section 5.4. Chapter 6 anticipates the total costs of such a system in order to find its Levelized Cost of Energy (LCOE), based on the prospected production of the previous chapter. Chapter 7 sets some considerations about the ground area usage of a kite wind farm and its organization possibilities.

Chapter 2

Airborne Wind Energy Systems

AWES are electro-mechanical machines that transform wind kinetic energy into electrical energy and are composed by a mechanically and/or electrically connected ground station and aircraft. These systems can be divided into Ground Generation (GG-AWES) or Flying Generation (FG-AWES) systems. As the name implies, ground generation systems convert mechanical to electrical energy on the ground while the latter do this conversion on the aircraft transmitting it through an electrical connection to the ground [8].

In Section 2.1 there is a description of existing Ground Generation concepts, and in Section 2.2 of Flying Generation possibilities. Section 2.3 consists of a review of existing AWES companies and research groups.

2.1 GG-AWES

GG-AWES produce electricity through mechanical work done by a traction force transmitted through the tether(s). There are several possibilities for this kind of systems, usually divided into fixed or moving ground station devices.

Fixed ground station devices, or Pumping Kite Generators (PKG), are systems based on a two- phased cycle, consisting in a generation phase and a retraction phase. A PKG system usually relies on a tethered airfoil whose tether is reeled around a winch drum connected to the axis of a generator.

During the generation phase, the airfoil is controlled in a way that it produces a Lift force, unwinding the tether and forcing the rotation of the generator axis, therefore inducing an electromotive force on the alternator terminals. To maximize the Lift force, the airfoil is set into a crosswind flight regime, since this creates a stronger wind apparent velocity [9]. The airfoil path is desirably elliptical or it follows an eight-shape (Bernoulli's Lemniscate), since this trajectory maximizes the time in which the kite is moving in an almost crosswind regime.

During the recovery phase, the generator works as a motor winding the tether and positioning the airfoil in its initial point. In this phase, the airfoil is controlled in order to minimize the traction force on the tether, thus reducing the energy needed to feed the motor.

The control system is crucial to guarantee that the aerodynamic characteristics of the airfoil maximize the power output during the first phase and minimize the power consumption during the recovery phase.

This state of operation has long alternating periods, requiring electrical rectification and a large capacitor, or similar, in order to deliver a stable power output to the grid.

Moving ground station systems aim to provide a more stable power output than the PKG, simplifying the connection to the grid. In these systems, the electric power generation is based on the ground station movement rather than the unwinding of a rope.

There are two kinds of moving ground station systems, the vertical axis generator and the rail generators. The first one consists on aircrafts connected to the periphery of a large generator with a vertical axis and force its rotation, producing torque and thus inducing electrical energy. The second system, inspired on Pocock's Charvolant [10], can be an open or closed loop rail system and is based on the movement of a railed vehicle. The motion of this vehicle, propelled by the traction force of an aircraft, generates electric energy.

2.2 FG-AWES

FG-AWES allow a more stable power output, only consuming energy while landing or taking-off and avoiding a two-phased cycle. However, there are complications generating power on the aircraft such as its weight increase and the necessity of transmitting electrical energy to the ground without a fixed structure. FG-AWES produce electricity in the air and there are several different solutions for the flying principles of each system, from solutions based on the lift of an airfoil with generators attached to it to the buoyancy of lighter-than-air structures.

2.3 AWES Under Development

Around the world there are an increasingly large number of research groups and companies developing different concepts of AWES, being the PKG the most explored. Figure 2.1 represents a world map with the location of active academic and entrepreneurial projects regarding AWES.

2.3.1 GG-AWES Under Development

In the Netherlands start-ups such as e-Kite [12] and AmpyxPower [13] have been developing prototypes based on a pumping cycle mechanism with rigid wings structures.

The model e-Kite aims to launch is the e100, seen in Figure 2.2, a fully autonomous system with $100kW$ nominal power that can be easily transported to remote locations. After the launch of the e100, e-Kite aims to scale the technology into a $500kW$ system.

AmpyxPower has been constructing its third prototype, AP3, with launch and landing capabilities and with an aircraft consisting of a wing with $12m^2$ surface area and two fuselages with the control and electronic systems incorporated. Before the launching of a commercial product,

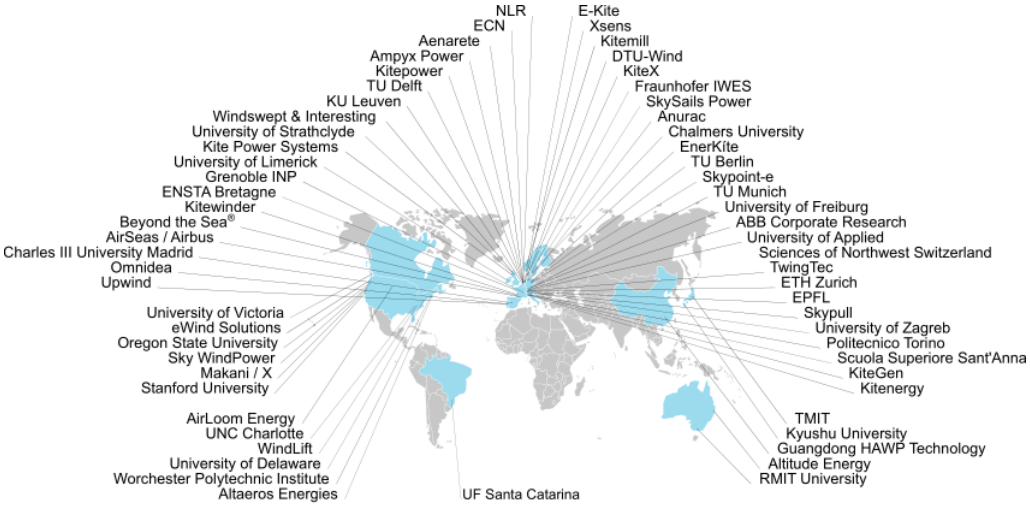

Figure 2.1: Institutions With Airborne Wind Energy Projects [11].

Figure 2.2: e-Kite e100 System [12].

Figure 2.3: Enerkite ek30, 30kW System [15].

AmpyxPower intends to develop its fourth generation prototype, AP4, with an intended 2MW capacity.

Also developing PKG systems, the Italian company KiteGen has been establishing a semi-rigid airfoil concept. The latest prototype, KiteGen Stem, consisted in a 3MW system [14].

A final corporate developed fixed ground station example is Enerkites products, varying from 30, 100 and 500kW of rated power. The three systems are based on swept rigid wings airfoils. Figure 2.3 presents the ek30 model [15].

Besides companies, several academic research groups are worth mentioning, such as TU Delft KitePower [16], Freiburg University and the recent group from University of Porto, UPWIND [1], to which this dissertation is associated. All three research groups focus on PKG systems.

Regarding moving ground station systems, KiteGen is also exploring a multiple kite system based on a vertical axis concept named KiteGen Carousel, shown in figure 2.4[14].

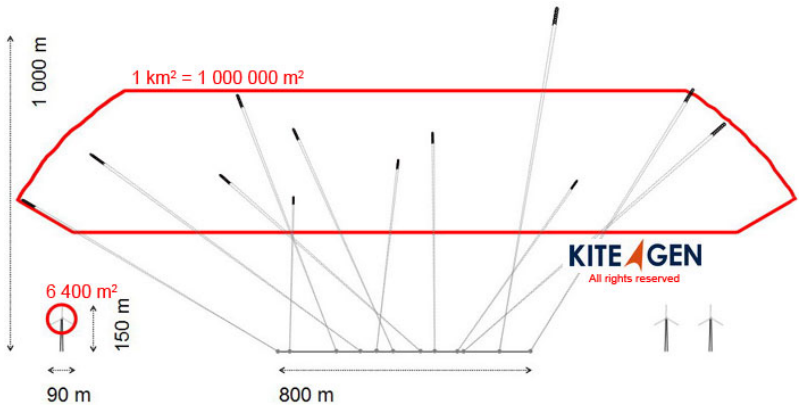

Figure 2.4: KiteGen Carousel [14].

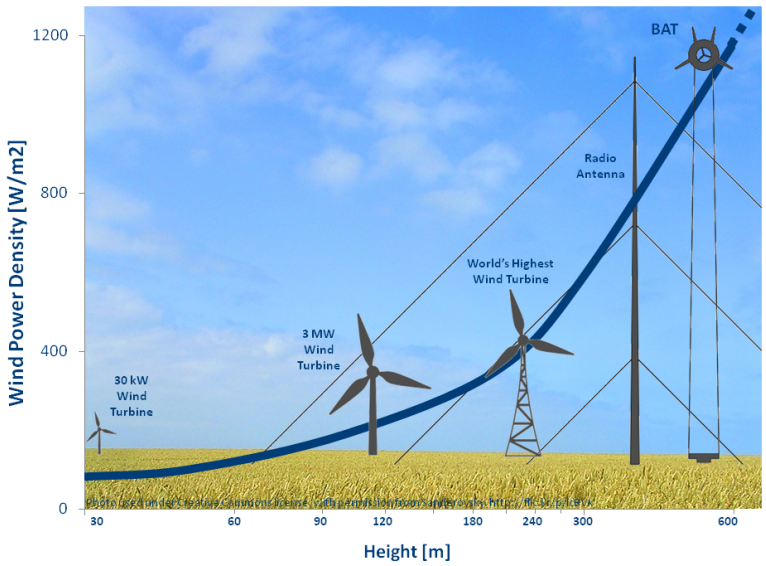

Figure 2.5: Altaeros Buoyant Airborne Turbine (BAT)[18].

2.3.2 FG-AWES Under Development

Regarding FG systems, Makani [17], in the USA, has launched in 2016 its M600 system, a rigid winged kite incorporating eight rotors that drive permanent magnet generators. This system has reached a 600kW rated power.

Also in the USA, Altaeros [18] elaborated its Buoyant Airborne Turbine system based on a floating platform holding a light-weight wind turbine that reaches heights up to 600m. In figure 2.5 is illustrated a comparison of this system with conventional wind turbines heights.

In Portugal, a lighter than air cylindrical aerostat, developed by Omnidea, that explores the Magnus effect can be used for electricity generation among other applications[19].

Chapter 3

Dynamic Model of the Kite Power System

A PKG system, introduced in the previous chapter, is composed by an aircraft, a kite-line (tether), a winch drum, a generator and electronic components necessary for the grid connection and energy output regulation.

The possible kites vary in shape and material and are characterized by the area (A), Lift and Drag coefficients (c_L and c_D) and mass (m). There are several rigid or flexible possibilities. This dissertation will focus on a rigid winged glider.

The model chosen to describe the kite dynamics is described in this chapter. Section 3.1 presents the chosen coordinate systems and Section 3.2 describes the forces acting on the kite. Finally, Section 3.3 states the dynamic equations.

3.1 Coordinate System

In order to model the forces and motion of the kite, we use three distinct coordinate systems: a global (G), a local (L) and a body (B) coordinate system.

- **Global** G - The first one is an inertial Cartesian coordinate system defined by (x, y, z), where the origin coincides with the ground station of the PKG and $\vec{\mathbf{e}}_x$ is aligned with the wind velocity.

- **Local** L - The local coordinate system is a non-inertial spherical coordinate system defined by ($\vec{\mathbf{e}}_r$,$\vec{\mathbf{e}}_\phi$,$\vec{\mathbf{e}}_\beta$).

- **Body** B - The last coordinate system is a non-inertial coordinate system defined by ($\vec{\mathbf{e}}_1, \vec{\mathbf{e}}_2, \vec{\mathbf{e}}_3$), where $\vec{\mathbf{e}}_1$ corresponds to the longitudinal axis of the aircraft, $\vec{\mathbf{e}}_2$ is an orthogonal axis to the first one pointing towards the left wing of the kite and $\vec{\mathbf{e}}_3$ is aiming upwards.

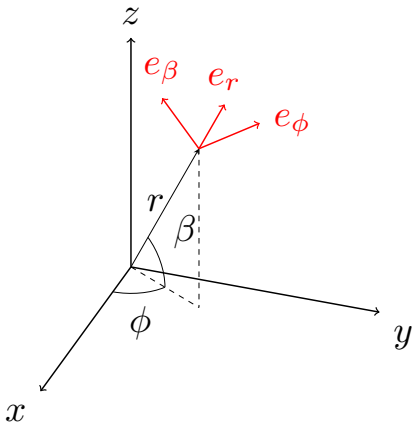

Figure 3.1: Global and Local Coordinate Systems.

Considering the position $\mathbf{p}$ describing the kite mass-point:

$$\mathbf{p} = \begin{bmatrix} x \\ y \\ z \end{bmatrix} = \begin{bmatrix} r\cos(\beta)\cos(\phi) \\ r\cos(\beta)\sin(\phi) \\ r\sin(\beta) \end{bmatrix},$$

the rotation matrix from L coordinate system to G is

$$\mathrm{R_{LG}} = \begin{bmatrix} \vec{\mathbf{e}}_r & \vec{\mathbf{e}}_\phi & \vec{\mathbf{e}}_\beta \end{bmatrix} = \begin{bmatrix} \cos(\beta)\cos(\phi) & -\sin(\phi) & -\sin(\beta)\cos(\phi) \\ \cos(\beta)\sin(\phi) & \cos(\phi) & -\sin(\beta)\sin(\phi) \\ \sin(\beta) & 0 & \cos(\beta) \end{bmatrix}$$

and the rotation matrix from G coordinate system to L is found to be $\mathrm{R_{GL}} = \mathrm{R_{LG}^{-1}} = \mathrm{R_{LG}^{\top}}$.

Considering the apparent wind velocity $\mathbf{v}_a = \mathbf{v}_w - \dot{\mathbf{p}}$. We assume that its radial component $\mathbf{v}_{a,r}$ is strictly positive [20] and that the kite body longitudinal axis aligns naturally with the apparent wind velocity, that is $\vec{\mathbf{e}}_1 = -\mathbf{v}_a/\|\mathbf{v}_a\|$.[21]

Being ψ the roll angle measuring rotation around the longitudinal axis ($\vec{\mathbf{e}}_1$) and considering that $\tilde{e}_2 = \vec{\mathbf{e}}_2$ (for $\psi = 0$) is initially in the plane τ, tangent to a sphere centred at the origin (containing the axis $\vec{\mathbf{e}}_\phi$ and $\vec{\mathbf{e}}_\beta$), we have that $\tilde{e}_2 \perp \vec{\mathbf{e}}_r$, and $\tilde{e}_2 \perp \vec{\mathbf{e}}_1$. Thus, we can define $\tilde{e}_2 = \dfrac{\vec{\mathbf{e}}_r \times \vec{\mathbf{e}}_1}{\|\vec{\mathbf{e}}_r \times \vec{\mathbf{e}}_1\|}$.

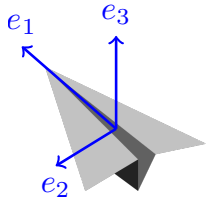

Figure 3.2: Body Coordinate System.

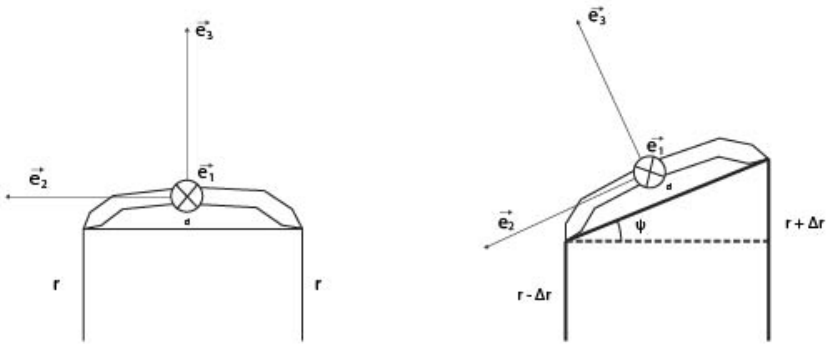

Figure 3.3: Roll Angle Variation for a Two Line Kite.

Finally, we consider the kite body has an anti-clockwise rotation of ψ around the $\vec{\mathbf{e}}_1$ axis: the roll angle. Since the kite has some mass, it would be necessary to control the angular acceleration, and consequently the angular velocity and roll angle. However, since the rotation of the kite is much faster than its translational movement in the defined operational range, we can consider, as a simplification, that the roll angle ψ can be controlled directly [1].

For example, in a two line kite where d is the distance between attachment points and Δr is the relative difference between the lengths of each line, as presented in Figure , we have $\sin\psi = \Delta r/d$ [22]. Using Rodrigues' formula to rotate $\tilde{e}_2$ by ψ around $\vec{\mathbf{e}}_1$, we obtain

$$\vec{\mathbf{e}}_2 = \tilde{e}_2\cos\psi + (\vec{\mathbf{e}}_1 \times \tilde{e}_2)\sin\psi + \vec{\mathbf{e}}_1(\vec{\mathbf{e}}_1 \cdot \tilde{e}_2)(1-\cos\psi) \tag{3.1}$$

and finally, we define $\vec{\mathbf{e}}_3$ as $\vec{\mathbf{e}}_3 = \vec{\mathbf{e}}_1 \times \vec{\mathbf{e}}_2$.

3.2 Acting Forces

Based on the definition of $\mathbf{p}$, we can calculate the respective velocity and acceleration through the demonstration in Appendix A, thus defining the total force acting on the kite as:

$$m\ddot{\mathbf{p}} = \vec{\mathrm{F}}^{\mathrm{th}} + \vec{\mathrm{F}}^{\mathrm{grav}} + \vec{\mathrm{F}}^{\mathrm{aer}}(\alpha). \tag{3.2}$$

The aerodynamic forces that act on the kite, Lift and Drag, depend on the squared apparent wind velocity and the angle of attack (α).

$$\vec{\mathrm{F}}^{\mathrm{aer}}(\alpha) = \frac{1}{2}\rho A\|\mathbf{v}_a\|^2(c_{\mathrm{L}}(\alpha)\vec{\mathbf{e}}_3 - c_{\mathrm{D}}(\alpha)\vec{\mathbf{e}}_1) \tag{3.3}$$

The angle of attack consists in the angle between the wind apparent velocity and the wing chord line (line connecting the trailing and the leading edge of the wing). Figure 3.4 depicts the angle of attack.

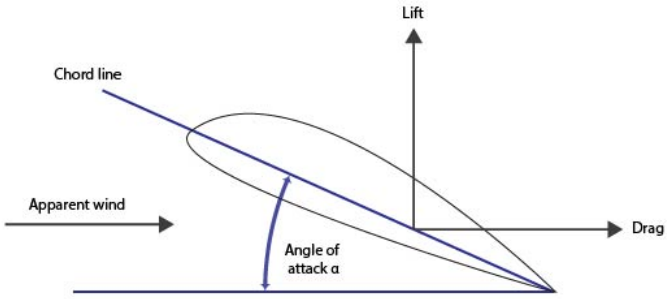

Figure 3.4: Angle of Attack.

In 1980, Miles Loyd [9] demonstrated that a crosswind motion was the best way to exploit the possibility of a PKG to utilize the wind kinetic energy, being this the way to maximize the apparent velocity of the wind and consequently the tension force on the tether, since this is highly dependent on the resultant aerodynamic force.

The tether tension force and gravity can be described as,

$$\vec{\mathrm{F}}^{\mathrm{th}} = -T\,\vec{\mathbf{e}}_r = \begin{bmatrix} -T \\ 0 \\ 0 \end{bmatrix}_{\mathrm{L}} \tag{3.4}$$

$$\vec{\mathrm{F}}^{\mathrm{grav}} = -mg\,\vec{\mathbf{e}}_z = \begin{bmatrix} 0 \\ 0 \\ -mg \end{bmatrix}_{\mathrm{G}} = \begin{bmatrix} -mg\,\sin\beta \\ 0 \\ -mg\,\cos\beta \end{bmatrix}_{\mathrm{L}}. \tag{3.5}$$

Where T represents the tension force at the ground station. These acting forces are represented in Figure 3.5.

In the Local coordinate system

$$\ddot{\mathbf{p}} = \begin{bmatrix} \ddot{r} \\ r\ddot{\phi}\cos(\beta) \\ r\ddot{\beta} \end{bmatrix}_{\mathrm{L}} + \underbrace{\begin{bmatrix} -r\dot{\beta}^2 - r\dot{\phi}^2\cos^2(\beta) \\ 2\dot{r}\dot{\phi}\cos(\beta) - 2r\dot{\phi}\dot{\beta}\sin(\beta) \\ 2\dot{r}\dot{\beta} + r\dot{\phi}^2\cos(\beta)\sin(\beta) \end{bmatrix}_{\mathrm{L}}}_{-\frac{1}{m}\vec{\mathrm{F}}^{\mathrm{inert}}}, \tag{3.6}$$

where the second parameter corresponds to the Coriolis and centrifugal forces, stated as inertial forces ($\vec{\mathrm{F}}^{\mathrm{inert}}$), and allowing us to redefine Newton's second law of motion as

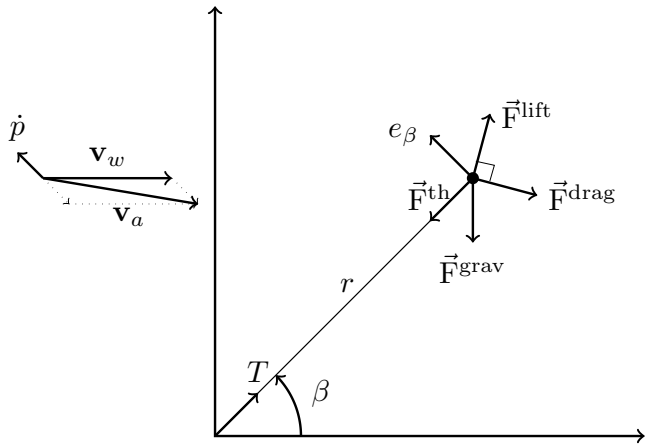

Figure 3.5: Acting Forces.

$$m\begin{bmatrix} \ddot{r} \\ r\ddot{\phi}\cos(\beta) \\ r\ddot{\beta} \end{bmatrix} = \vec{\mathrm{F}}^{\mathrm{th}} + \vec{\mathrm{F}}^{\mathrm{grav}} + \vec{\mathrm{F}}^{\mathrm{aer}}(\alpha) + \vec{\mathrm{F}}^{\mathrm{inert}}. \tag{3.7}$$

3.3 Dynamic Model

Assuming that the radial acceleration can be directly controlled by a_t, we can define the state variables $\mathbf{x} = \left(r, \phi, \beta, \dot{r}, \dot{\phi}, \dot{\beta}\right)$, the control variables $\mathbf{u} = (a_t, \alpha, \psi)$ and the dynamic equation of the system as:

$$\dot{\mathbf{x}}(t) = f(\mathbf{x}(t), \mathbf{u}(t)) = \frac{\mathrm{d}}{\mathrm{d}t}\begin{bmatrix} r \\ \phi \\ \beta \\ \dot{r} \\ \dot{\phi} \\ \dot{\beta} \end{bmatrix} = \begin{bmatrix} \dot{r} \\ \dot{\phi} \\ \dot{\beta} \\ a_t \\ \dfrac{1}{mr\cos(\beta)}\mathrm{F}_\phi \\ \dfrac{1}{mr}\mathrm{F}_\beta \end{bmatrix}$$

where F_ϕ and F_β are the resultant force components in $\vec{\mathbf{e}}_\phi$ and $\vec{\mathbf{e}}_\beta$ respectively.

The model described in this chapter is used to construct the Matlab/Simulink models to simulate the PKG dynamics.

Chapter 4

Kite Power System Simulation

In order to simulate the quasi-steady motion of the kite for different settings, a Matlab/Simulink Model was designed based on the dynamic model presented in Chapter 3. Parting from the state variables $\mathbf{x}$, the Inertial and Gravitational Forces are directly computed through equations (3.2) and (3.5) . The state variables are also used as an input for the controller which defines the three control variables (α, ψ, a_t). The control variables α and ψ define amplitude and direction of the Aerodynamic Forces, as described by equation (3.2), and its regulation varies according to the phase the Kite Power System is currently on. Through the Newton's Second Law of Motion, the acceleration for different coordinates is computed and integrated, showing the new state variables. The Power output of the system is calculated as the product between Tether Tension Force and the radial velocity. This simulation project was adapted for an over-view of an Underwater Kite motion and a side-view and three-dimensional analysis of a Kite Power System.

Firstly, an underwater kite system is explored through an overview of its motion in Section 4.1. Section 4.3 analyses the 2D motion of the kite for different wind speed conditions and concludes with a side-view of the kite movement through a complete production cycle. The description of the 3D model with the respective trajectory controller and wind gust response system and the resultant simulation results is in Section 4.4.

Appendix B shows a closer look at the 3D Matlab/Simulink Model Subsystems. An in-depth analysis of the underwater and 2D Matlab/Simulink systems is not displayed, since these can be derived from the 3D model.

4.1 Underwater Kite

The same principle explained for a KPS applies for other fluids such as water. Instead of using the kinetic energy of air masses, the same principle can be applied to water streams. Although, in this case, the stream speed is generally smaller than common wind speeds, the water density is around 800 times larger than the air density, reaching equivalent, if not larger, power outputs.

In order to explore the control capabilities of the azimuth angle (ϕ) of a kite, we have developed a simulation of an Underwater kite system based on the system described in [23].

Since the objective of this simulation is the control of the azimuth angle, the elevation of the system will be ignored. Therefore, the system will only be analyzed in a two-dimensional view, specifically an overview of the kite motion, neglecting the elevation angle and vertical components of forces.

The characteristics of the Underwater Kite are similar to a plain board and differ widely from the kite used on the following simulations. The system and simulation parameters are shown in Table 4.1.

Table 4.1: Underwater Kite Simulation Parameters

Parameter	**Value**
ρ	$1000\ kg\ m^{-3}$
v_w	$5\ ms^{-1}$
m	$100\ kg$
A	$10\ m^2$
AR	2

The relation between the lift and drag coefficients and the angle of attack is represented by the following expressions:

$$c_L(\alpha) = \frac{2\pi\alpha}{1+\frac{2\alpha}{AR}} \tag{4.1}$$

$$c_D(\alpha) = 1.28sin(\alpha) + \frac{c_L(\alpha)^2}{0.7\pi AR}. \tag{4.2}$$

In this simulation, during the production phase, the control method consists in altering an angle correspondent to ψ, as defined in Section 3.1 for a three-dimensional model, so that ϕ reaches a maximum or a minimum value. When a maximum tether length is reached, the underwater kite is centred by the same control methodology and is retrieved.

For the simulation of an underwater kite motion, the Matlab/Simulink model presented in Figure 4.1 is used. The starting conditions were a fluid speed of $5m/s$, a tether length varying from 20m to 250m and ϕ between -20^o and 20^o. Figure 4.3 shows the evolution of the tether length, the azimuth angle and the roll angle through an $1800s$ simulation and the resultant motion of the underwater kite is described in Figure 4.2.

4.2 Elevation variation with the Angle of Attack and Wind Speed

For a given kite with a constant tether length and angle of attack, there is a natural elevation angle depending on the wind velocity magnitude. In order to assess this characteristic for the kite parameters used on the following simulations, an adaptation of the existing simulation project was developed.

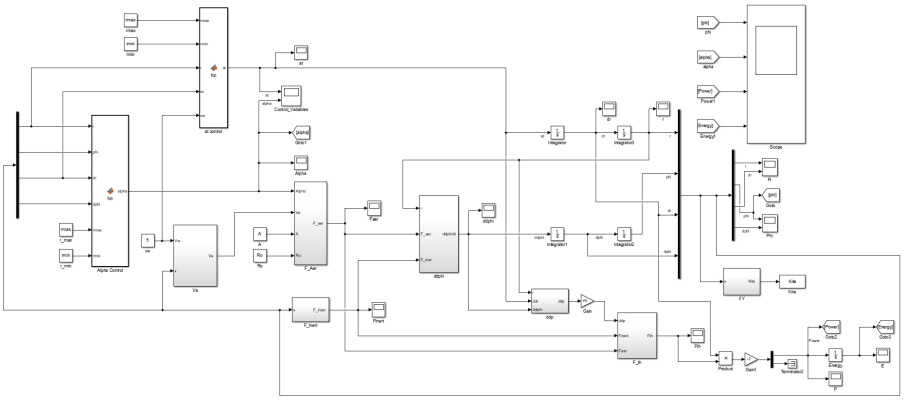

Figure 4.1: Underwater Kite Simulink Model.

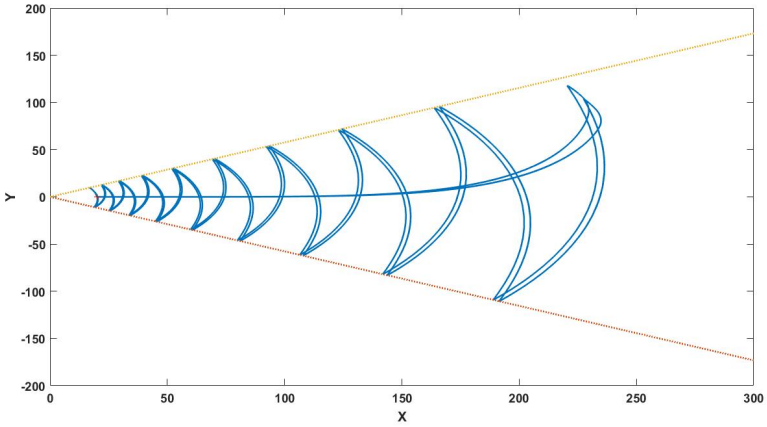

Figure 4.2: Underwater Kite Trajectory.

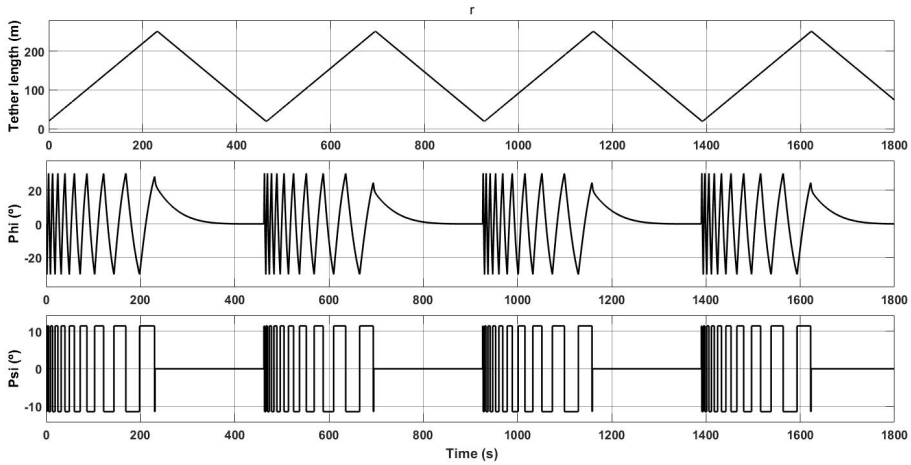

Figure 4.3: Underwater Kite State Variables (r, ϕ) and Control Variable (ψ).

The parameters chosen for the kite are shown in Table 4.2 and the lift and drag coefficients response to the angle of attack is presented in the succeeding equations.

$$\begin{cases} c_L(\alpha) = 0.3 + 0.1\alpha \ , \ 0^o < \alpha < 12^o \\ c_L(\alpha) = 9.9 - 0.7\alpha \ , \ 12^o < \alpha < 15^o \end{cases} \tag{4.3}$$

$$c_D(\alpha) = 0.012 + 0.01\alpha \tag{4.4}$$

Table 4.2: 2D Simulation Parameters

Parameter	**Value**
ρ	$1.2\ kg/m^3$
v_w	$10\ m/s$
g	$9.8\ m/s^2$
m	$0.7\ kg$
A	$0.28\ m^2$

The coefficients variation with α was taken from a linearization of a [24] graphic and, therefore, is a mere approximation of a real characteristic.

Table 4.3 shows the values for the elevation and stabilization wind speed for different angles of attack. The elevation wind speed, for a given angle of attack, consists in the value for which the lift force equals the weight of the kite, thus starting to elevate it. Between these two values the kite presents an oscillatory movement without noticeable attenuation, since the drag force for a given angle of attack in this wind speed range is not capable of attenuating this oscillatory response. Therefore, the stabilization wind speed consists in the value for which the drag force is sufficient to totally damp this oscillatory response. With an increasing angle of attack the oscillations demonstrate a reduced amplitude and last for a smaller range of wind speeds, since the drag force is larger for larger values of α.

Figures 4.4 and 4.5 represent the variation of β for different angles of attack and wind speeds. The dashed lines represent the maximum and minimum values observed and allow us to interpret the range of values in which the oscillations are noticeable.

The natural elevation angle tends to a small range of values and the effect of the different angles of attack seem to be negligible. For these given parameters this elevation angle is above 80^o. This natural elevation depends on $tan^-1(\frac{c_L}{c_D})$, therefore the final elevation angle shown for $\alpha = 13^o$ is lower than the others, since its lift coefficient is computed from a different $c_L(\alpha)$ characteristic.

Table 4.3: Natural Elevation Angle

α	**Elevation**	**Stabilization**
0^o	$11.6\ m/s$	$17.6\ m/s$
5^o	$7.1\ m/s$	$11.2\ m/s$
10^o	$5.6\ m/s$	$8.8\ m/s$
12^o	$5.2\ m/s$	$8.0\ m/s$
13^o	$7.1\ m/s$	$10.0\ m/s$

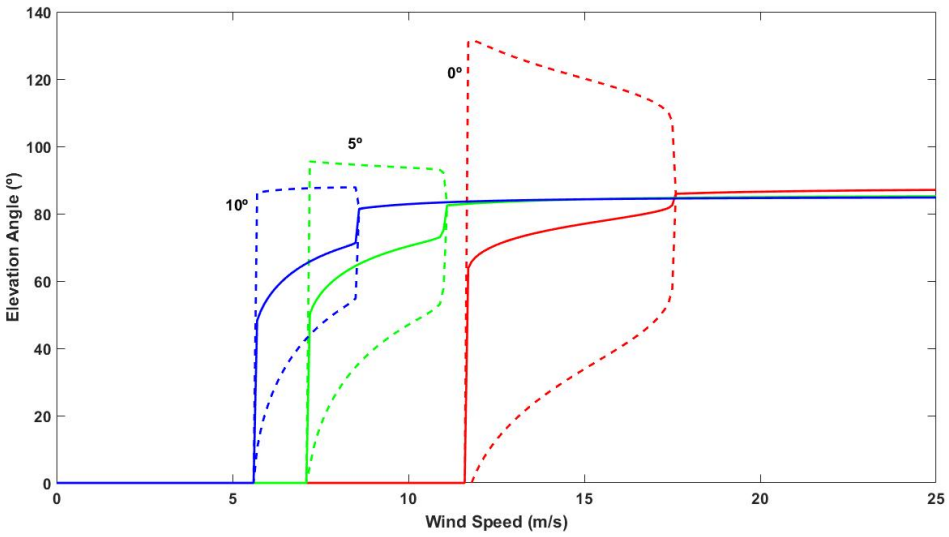

Figure 4.4: Variation of β for α Equal to $0^o, 5^o$ and 10^o.

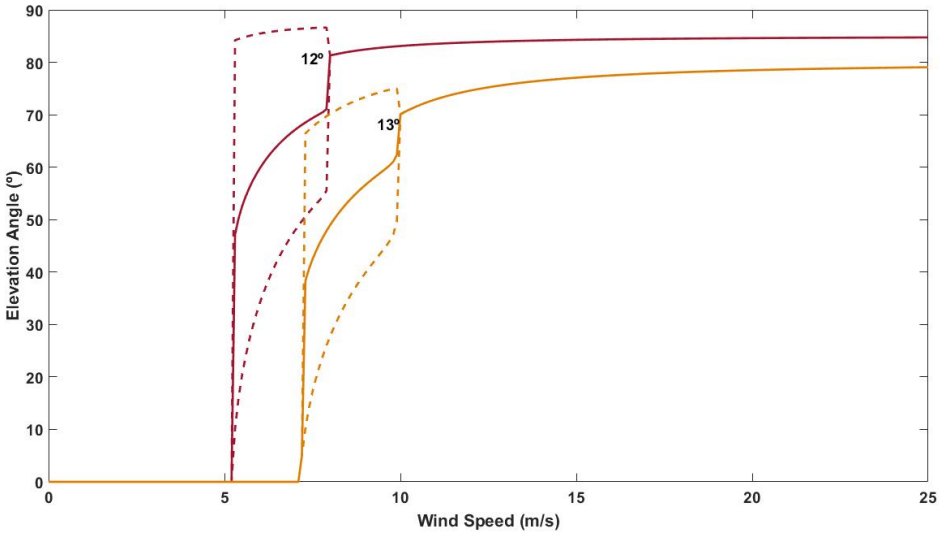

Figure 4.5: Variation of β for α Equal to 12^o and 13^o.

4.3 2D Simulation

In a 2D simulation, based on a side-view of the kite motion, the ϕ component was neglected ($i.e \phi = 0$). The analysis is then based only on β and r. The control variables are α and the tether unwinding acceleration. During the production phase, the desired motion consists on an almost sinusoidal variation of the elevation with a constant reel-out velocity. The control used consists in adjusting the angle of attack in order to vary β between a maximum and minimum value, that define the flight envelope of the kite. When the retraction phase is reached, the kite elevates to a defined β^* and the tether is reeled back onto the winch drum.

Figure 4.6 represents the resultant simulation for a wind velocity of $10m/s$, a tether length varying from 20m to 250m and β varying between 20^o and 60^o (represented by the two straight lines in the graph) in the production phase. Figure 4.7 displays the variation of the state variables r and β and the control variable α through the complete simulation. Figure 4.8 portrays the Matlab/Simulink model for the 2D simulation.

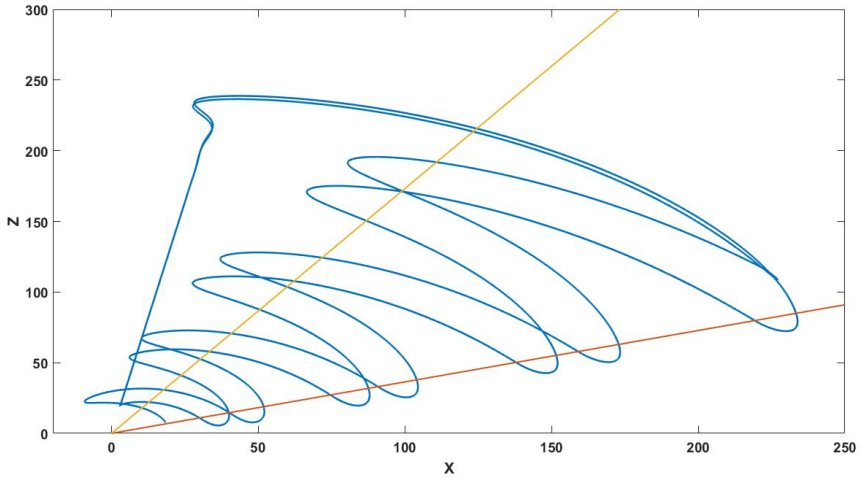

Figure 4.6: Complete Cycle for 2D Simulation.

4.4 3D Simulation

During the production phase the tether is reeled-out until it reaches a maximum tether length. In order to optimize power production and guarantee a constant and predictable behaviour, the kite follows a defined path. This path is intended to approach an almost crosswind motion. When the maximum tether length is reached, the tether must be retrieved in order to restart the production cycle. During the retraction phase, the kite is directed to a position in which $\phi = 0$ and elevated to a defined value of β while the tether is reeled back in.

All three-dimensional simulations presented use the same parameters shown in Table 4.2 and follow the same lift and drag coefficients response to α described by equations (4.3) and (4.4). Figure 4.9 depicts the Matlab/Simulink model for the 3D simulation.

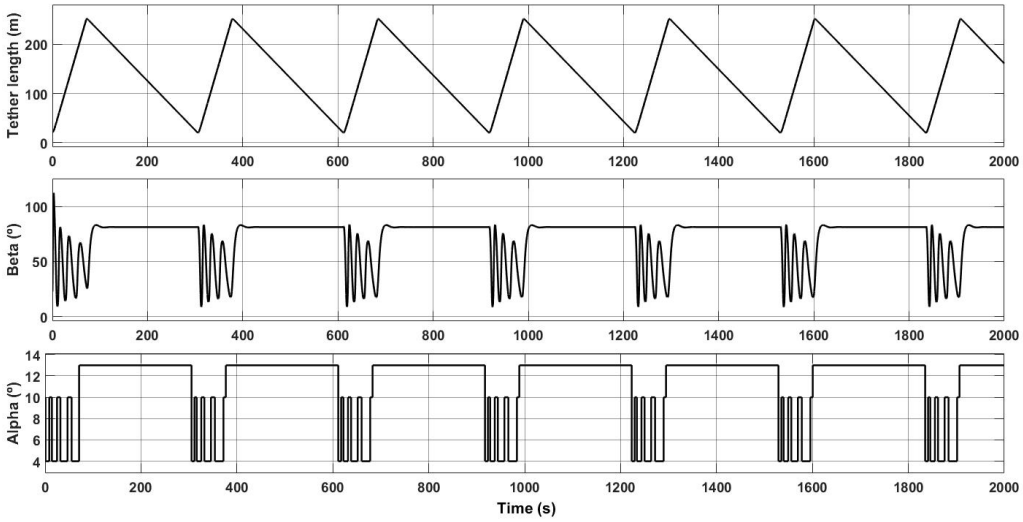

Figure 4.7: 2D Simulation State Variables (r, β) and Control Variable (α).

4.4.1 Trajectory Controller and Wind Gusts Response

The intended production phase path forms an almost elliptical shape, maximizing the periods in which the kite approaches a crosswind motion. The path is defined in the plane τ, hence only set in (ϕ, β), in order to make it independent of the tether length or reel-out velocity.

Considering a simplified kite mass-point position $\mathbf{p}(\phi, \beta)$, the closest point in the trajectory array (A) is calculated. Then, a reference target B is defined as the point distancing a certain distance from A in a forward direction in the desired path. An auxiliary vector is then defined as the vector between the mass-point position $\mathbf{p}$ and the reference target B. An angle (γ) between the auxiliary vector and the kite velocity serves as a direction reference to the kite, as demonstrated in Figure 4.10.

For the implementation of the trajectory controller in the Matlab/Simulink model, the desired path is set as an array of points in the τ plane and L_1 constitutes the number of indices in the referred array between the minimum distance point (A) and the target (B). A proportional controller for the roll angle (ψ) aiming to drive γ towards zero is set as $\psi(t) = K_\psi \gamma(t)$. A proportional controller is proven to be a suitable solution for the steering of the kite in [25].

Although this trajectory controller has shown to be robust to high wind speeds, the resultant tether tension force can be overwhelming for certain components of the system, such as the tether. Therefore, for safety purposes, a gust handling strategy is necessary. The chosen method consists in elevating the kite and centering it in $\phi = 0$ while interrupting the reeling of the tether. The angle of attack is increased, stalling the kite and avoiding undesired movements besides reducing the lift force and consequently the tether tension. When the wind velocity returns to acceptable values, the kite resumes to the production or retraction phase, depending on which phase was interrupted by the wind gust. Figures 4.11 and 4.12 demonstrate the trajectory controller and wind gust response for a constant tether length and a full production cycle, respectively.

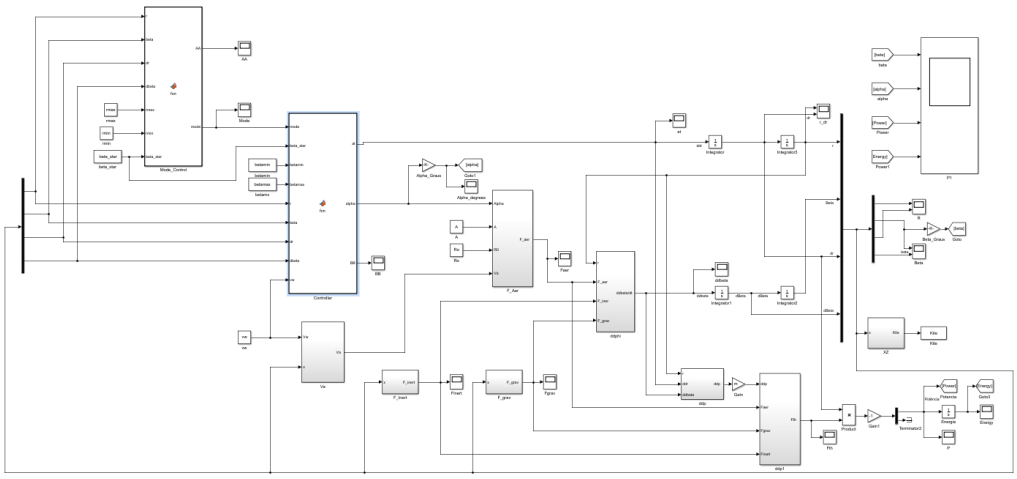

Figure 4.8: 2D Matlab/Simulink Model.

4.4.2 Simulation Results

4.4.2.1 Fixed Tether Length

In a fixed tether length simulation is noticeable the effect on limiting the tether tension force of the wind gust handling strategy. Figure 4.13 presents the variation of the tether tension radial component with wind speeds starting at $10m/s$, with an increase to $30m/s$ and finishing the simulation with $20m/s$. With an increase of the wind speed the amplitude and frequency of the tether tension variations increases as expected, and with a wind speed of $30m/s$ the peak tether tension reaches almost $20kN$.

With the incorporation of a wind gust handling strategy, with a wind speed threshold of $25m/s$, for the same simulation conditions, the tether tension during the period of $30m/s$ wind is limited reaching almost $0N$ and the peak tension is found for winds of $20m/s$ with forces above $8kN$, as depicted in Figure 4.14.

4.4.2.2 Complete Production Cycle

With a Complete Production Cycle, *i.e.*, with production and retraction phases in a quasi-steady regime, the reeling of the tether in the first phase varies with the current wind speed in order to maximize power production. Therefore, with an increasing wind speed the time in which the kite-line is being reeled-out decreases.

The Wind Gust response interrupts the pumping cycle phase and the reeling of the tether in the period between $200s$ and $250s$, as can be seen in Figure 4.15. After the wind gust, the kite resumes to the phase interrupted by the gust. For the case in Figure 4.15, the kite resumes to the production phase. During the retraction phase and wind gusts, the kite is elevated and centered, thus β is increased to a value around 80^{o} and ϕ equals zero.

The trajectory of a $2000s$ long uninterrupted simulation for a wind speed of $10m/s$ is shown in Figure 4.16 and Figure 4.17 describes the variation of ϕ and β during this simulation. The kite

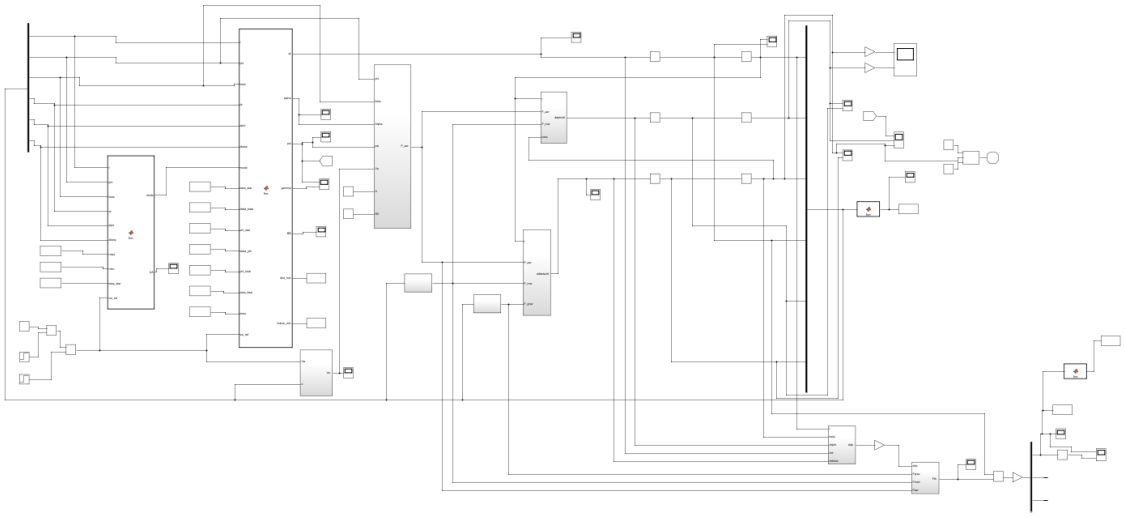

Figure 4.9: 3D Simulink Model.

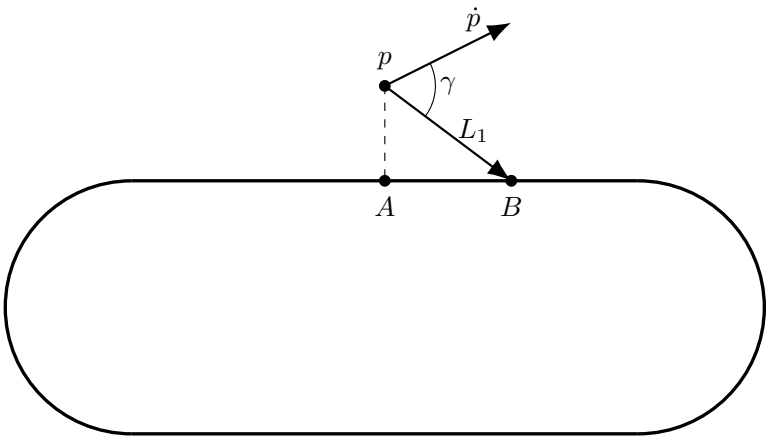

Figure 4.10: Trajectory Controller Schematic Figure.

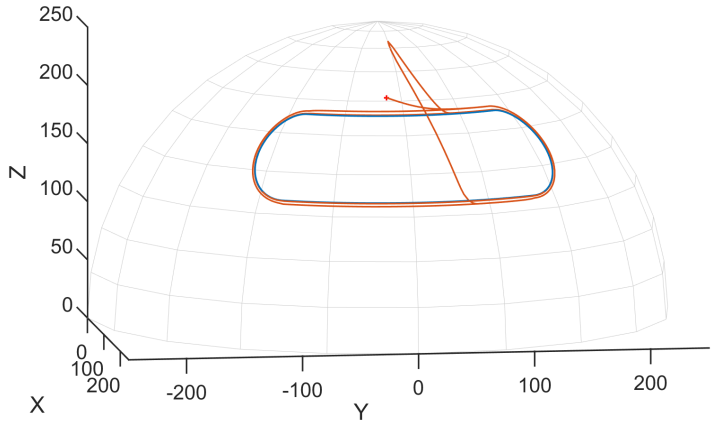

Figure 4.11: Follow Path with Constant Tether Length and Wind Gust Response.

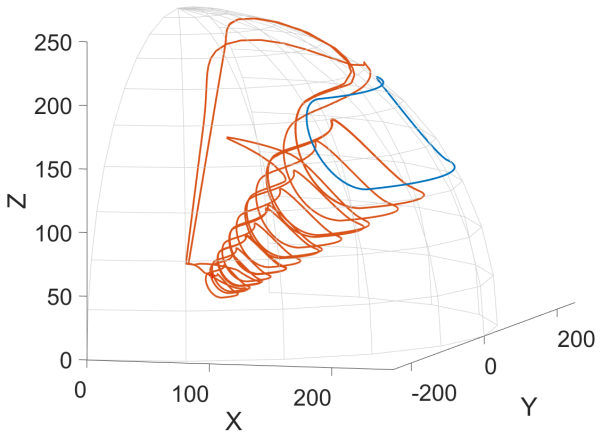

Figure 4.12: Follow Path with Full Production Cycle and Wind Gust Response.

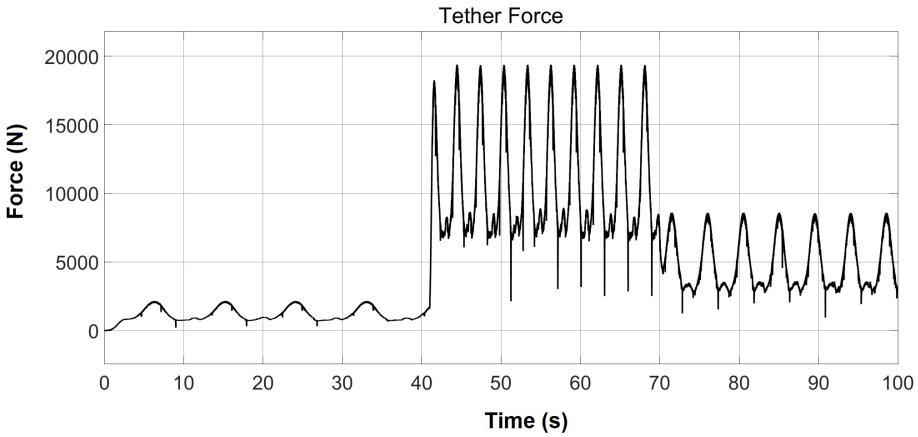

Figure 4.13: Tether Force with Fixed Tether Length and Without Wind Gust Response in a 100s Simulation.

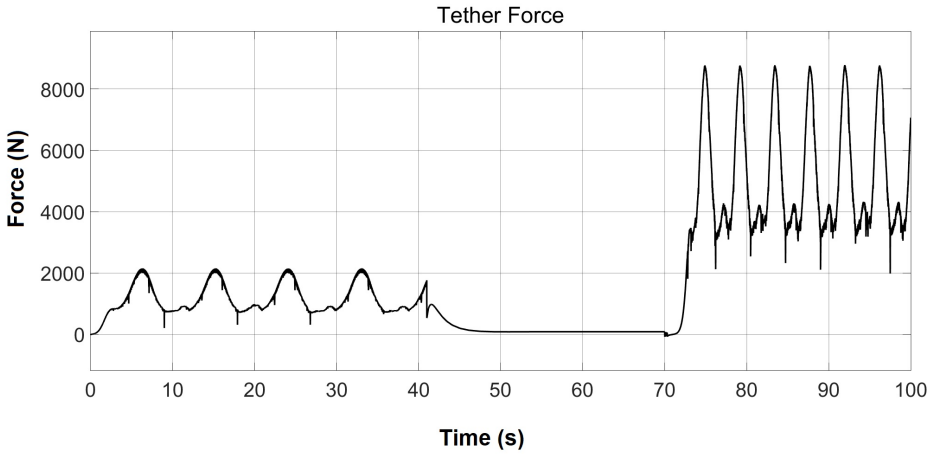

Figure 4.14: Tether Force with Fixed Tether Length and Wind Gust Response in a 100s Simulation.

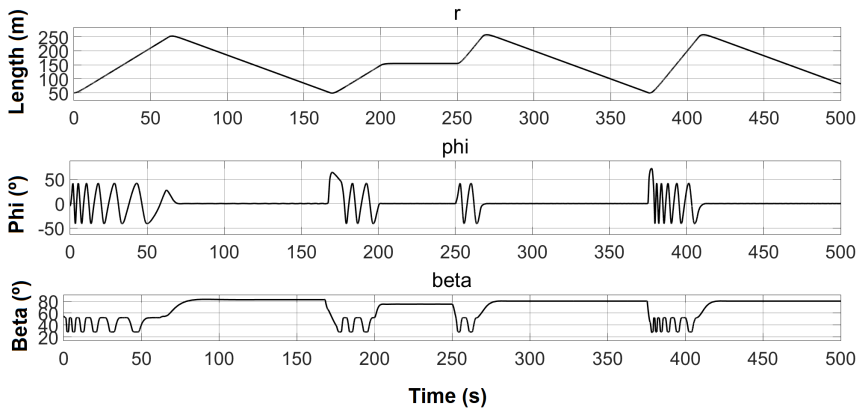

Figure 4.15: State Variables (r, ϕ, β) for a Complete Production Cycle with Wind Gust Response.

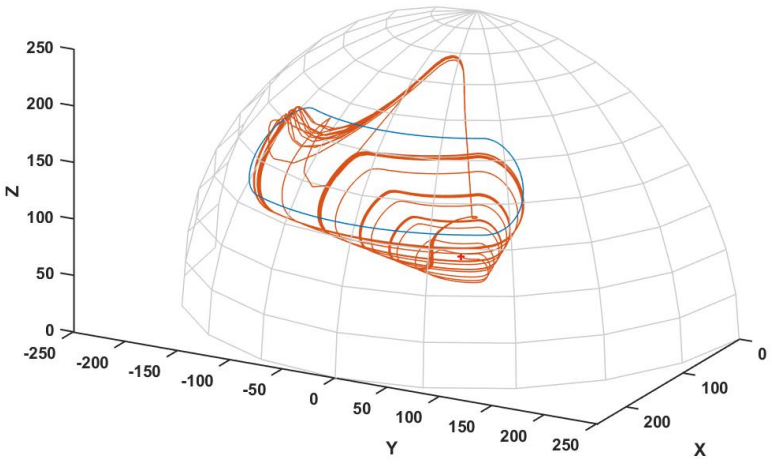

Figure 4.16: Complete Production Cycle Trajectory of a 2000s Simulation with $v_w = 10m/s$.

retraction phase radial velocity is set to $-2m/s$. The initial tether length is 50m long, but during the quasi-steady motion the tether length varies between 70m and 250m, as shown in the following table.

Table 4.4: Simulation Parameters and Conditions

Parameter	**Value**
v_w	10 ms^{-1}
r_0	50 m
r_{min}	70 m
r_{max}	250 m

Although there is power consumption during the retraction phase, the cumulative energy output is positive and the peak power reaches a value of around 3kW, as shown in Figure 4.18.

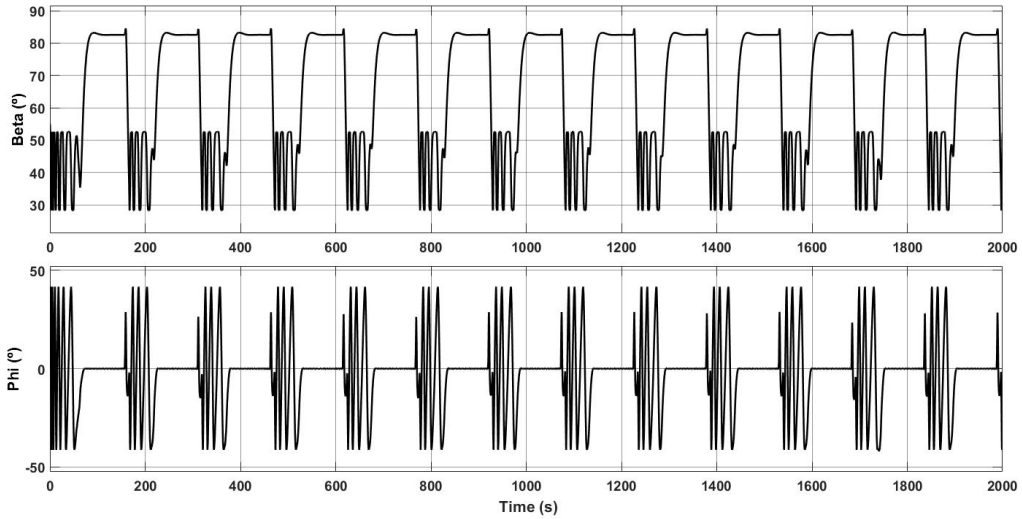

Figure 4.17: State variables (β, ϕ) of a 2000s Simulation With $v_w = 10m/s$.

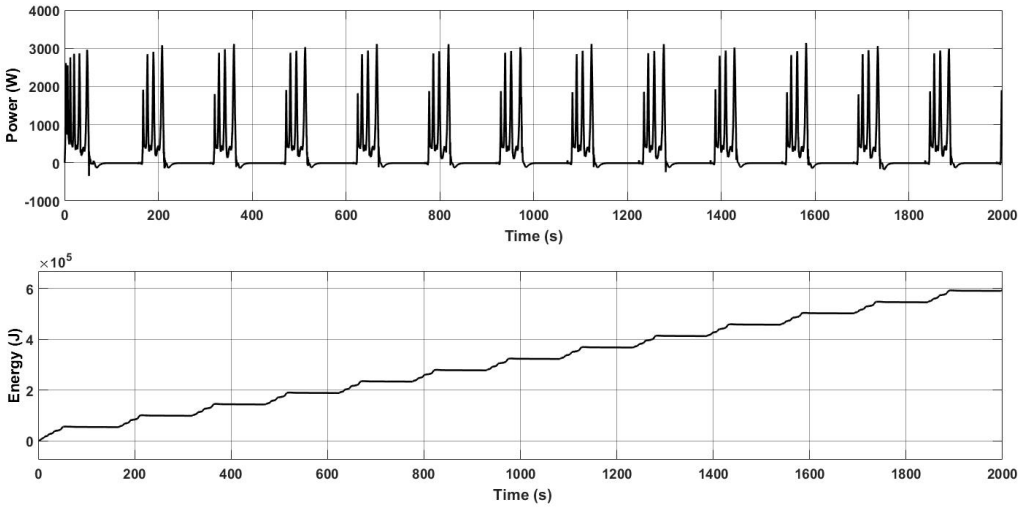

Figure 4.18: Power (W) and Energy (J) Output of a 2000s Simulation with $v_w = 10m/s$.

Chapter 5

Local Wind Characteristics and Power Curve Construction

This chapter explains a characterization of wind speed variations in a location and the construction of the power curve for the developed KPS.

Starting in Section 5.1 with an overview of the used procedure to model the wind, Section 5.2 uses the tools introduced in the preceding section to determine the characteristics of the chosen site.

Section 5.3 explains the empirical process through which the control parameters were chosen for varying wind speeds in order to guarantee a certain operation stability. Since several components of the system are sized for a given rated power, the power output found in Section 5.3 needs to be limited in order to estimate the power curve and consequent results such as capacity factor and estimated average power produced for the location chosen in Chapter 5. Section 5.4 explores the definition of the final power curve.

5.1 Wind Resource Characterization

Wind consists of air flow caused by pressure differences along the surface of the earth due to differences in solar radiation in different parts of the globe. It is stronger and more consistent at higher altitudes, since it is affected by surface friction at lower altitudes. Its velocity and direction vary strongly in time, with the weather and local terrain which forces the existence of long-term measurements for a reliable characterization of the wind in any location.

5.1.1 Power Spectral Density

Wind can be described in the frequency domain. Since wind characteristics vary widely with the location, a spectral analysis of the wind is only faithful to the reality where the measurements were made. However, it has been empirically verified that wind frequency characteristics are relatively constant.

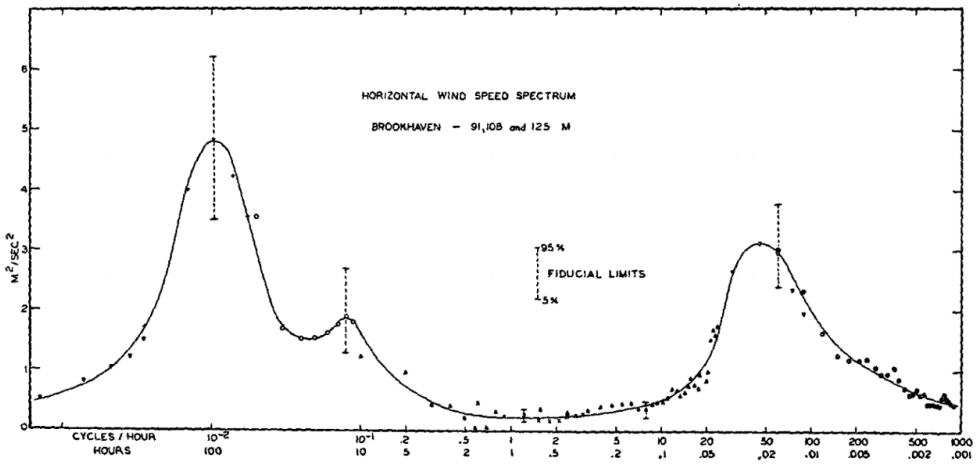

Figure 5.1: Typical Power Spectral Density [26].

Power Spectral Density (PSD) corresponds to a function of the kinetic power density of the wind, related to the horizontal component of the wind velocity. Typically, PSD functions reveal the existence of three distinctive zones. Two peaks of the function and a gap zone between them. These three zones are:

- **Macro-Meteorological Zone** - This zone is characterized by a peak at low-frequency wind speeds with periods of several days and is related with the flow of large masses of air created by synoptic-scale pressure systems.

- **Micro-Meteorological Zone** - This zone is characterized by a peak at high-frequency wind speeds with periods of a few seconds or minutes and it is associated with turbulence phenomena.

- **Spectral Gap Zone** - This zone stands between the micro and macro meteorological zones and is a large gap of low energy wind variations.

Figure 5.1 represents a typical spectral density of wind velocity, presented by [26].

The existence of the spectral gap zone allows us to simplify the analysis by dividing wind velocity in two components. A component related to low-frequency wind speeds and another one related with turbulence and high frequency variations. Mathematically, we can describe it as $v_w(t) = v_w + v'_w(t)$, in which v_w, represented as a constant, is the low-frequency component and $v'_w(t)$ corresponds to the high-frequency component, [27]. This separation, created by the Spectral Gap zone, allows to deal with the two high energetic components separately and analyze the turbulent winds as a disturbance in a quasi-steady flow defined by an average wind velocity, [28].

5.1.2 Speed and Power Relations

Another way to characterize a location is its annual mean wind speed. This value does not consider the variations of the wind. The annual mean wind speed allows us to compare two different sites and can be used to make a simple estimate of the wind power density at a certain location.

5.1.3 Weibull and Rayleigh Distribution

A statistical analysis of the wind speed can be described through a probability density function. Typically, the Weibull Distribution is considered the most appropriate function to portray wind speed variations. This distribution function is described by the following equation:

$$f(v) = \frac{k}{c}\left(\frac{v}{c}\right)^{k-1} e^{-\left(\frac{v}{c}\right)^{k}}. \tag{5.1}$$

In which k is a shape parameter and c is a scale parameter expressed in m/s.

Through this probability distribution function we can compute the annual mean speed by integrating the product of the actual wind speed measurements and the probability distribution.

The shape and scale parameters of the Weibull function are related to the wind speed characteristics, such as its annual mean speed and variance, through the Gamma (Γ) function. Being the wind annual mean speed (v_{wa}):

$$v_{wa} = c\Gamma\left(1+\frac{1}{k}\right), \tag{5.2}$$

k usually varies between 1.5 and 2.5. In this interval $\Gamma \approx 0,9$. This allows us to conclude that v_{wa} is usually 90% of c. For cases in which $k = 2$, with the same expressions shown above, the probability distribution function becomes a Rayleigh function. The Rayleigh function is useful for situations where there is not any experimental data and we aim to describe the wind speed probability distribution of a location only based on the annual mean wind speed, calculating the distribution scale parameter using the following expressions [28]:

$$\Gamma\left(1+\frac{1}{2}\right) = 0.88623, \tag{5.3}$$

$$c = \frac{v_{wa}}{0.88623}. \tag{5.4}$$

5.2 Local Characterization

5.2.1 Global Wind Atlas

The Global Wind Atlas (GWA), developed by the Technical University of Denmark (DTU), provides a combined public domain dataset of wind climate statistics with a high resolution, aiming to "clarify the role of wind energy in the future global energy mix" [29].

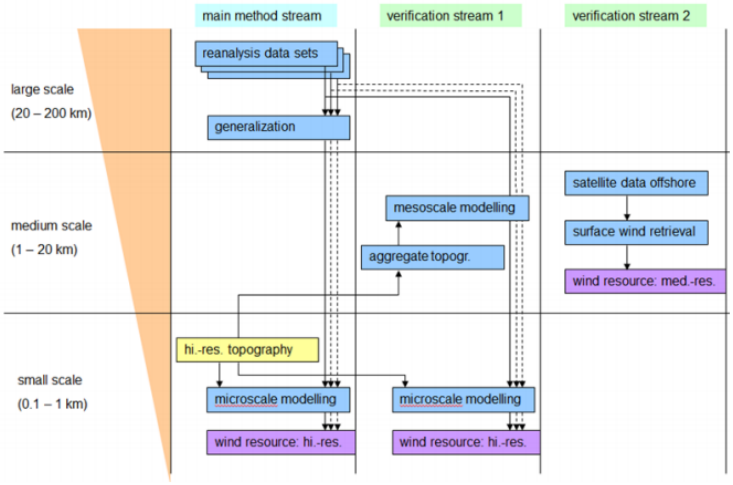

Figure 5.2: Global Wind Atlas Method [29].

GWA uses a down-scaling process parting from a large scale data set and ending up with a micro scale wind climate data. The large scale data has a resolution of about $50km$ and is provided by atmospheric reanalysis from meteorological centres spread around the world. The data acquired is then generalized to define a data set with an uniform resolution which is applied into a micro scale modelling system that computes local wind characteristics every $250m$ at heights of $50, 100$ and $200m$. The micro scale grid is aggregated, defining a final $1km$ spacing grid. Figure 5.2 shows a diagram presenting the GWA methodology.

5.2.2 Local Characterization

The location chosen to develop further studies is Praia do Cabedelo (Viana do Castelo, Portugal) with coordinates $4140'55.7"N 849'58.8"W$, as presented in Figure 5.3. Figure 5.4 shows a wind rose histogram with 30^o intervals from which we can derive the predominant wind direction.

Table 5.1 displays the annual average wind speeds for the chosen site and the correspondent scale parameters for the Rayleigh probability density function. Based on the annual average wind speeds, the desired scale parameters for the Rayleigh distribution is calculated using equation (5.4). Figure 5.5 shows the Gamma function and Figure 5.6 shows the resultant Rayleigh distribution for this location for altitudes of $50, 100$ and $200m$.

Table 5.1: Annual Average Wind Speeds and Scale Parameters for Altitudes of $50, 100$ and $200m$

Altitude	Annual Mean Wind Speed	Scale Parameter
$50\ m$	$6.46\ m/s$	$7.30\ m/s$
$100\ m$	$7.01\ m/s$	$7.91\ m/s$
$200\ m$	$7.63\ m/s$	$8.61\ m/s$

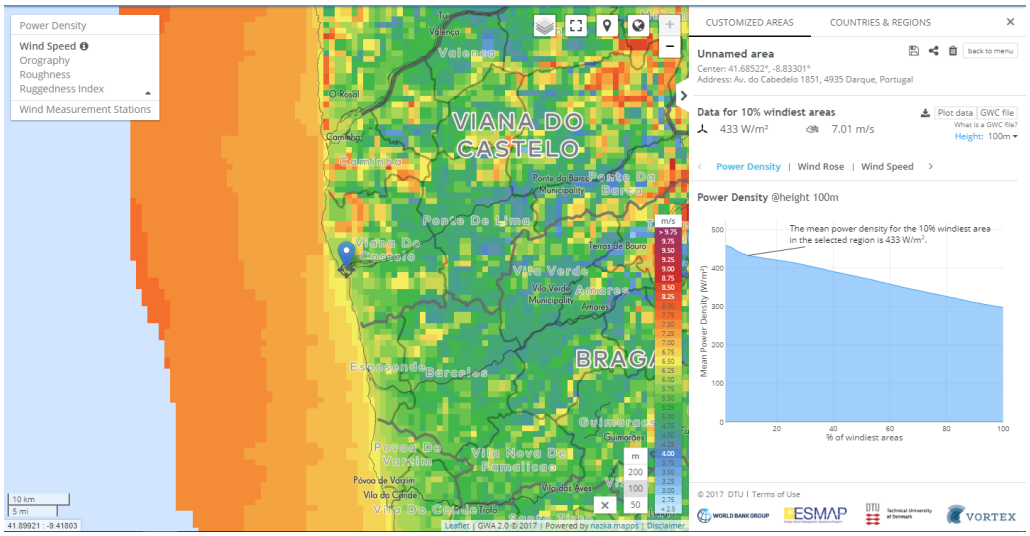

Figure 5.3: Praia do Cabedelo Characteristics [29].

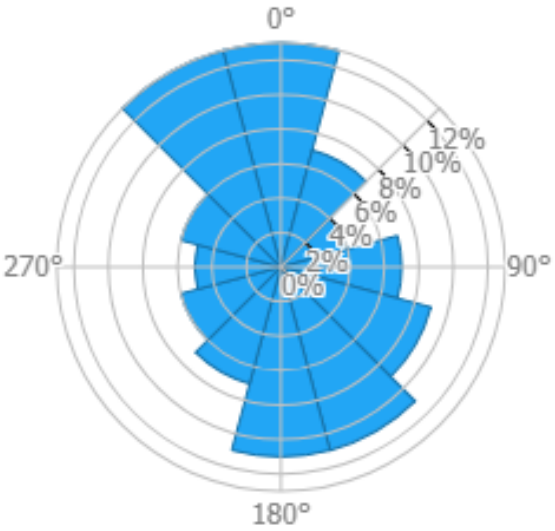

Figure 5.4: Predominant Wind Direction for Praia do Cabedelo [29].

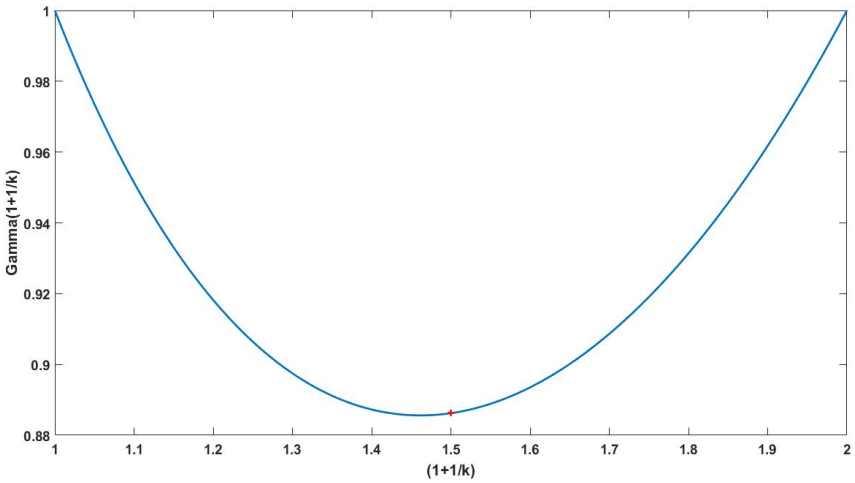

Figure 5.5: Gamma Function - $\Gamma\left(1+\frac{1}{k}\right)$.

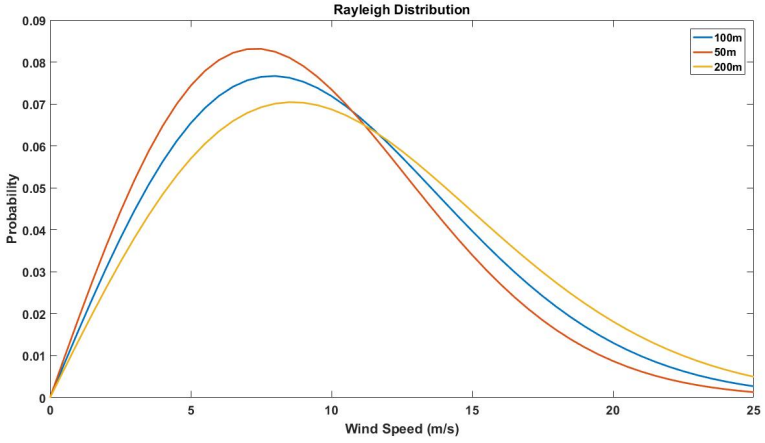

Figure 5.6: Rayleigh Probability Density Function For Praia do Cabedelo For Altitudes Of $50, 100$ and $200m$.

5.3 Empirical Selection of Parameters for Maximization of Energy Output

In order to achieve a working system for different wind speeds, certain parameters in the control methodology have to be adjusted. These parameters are the gain (K_ψ) for the ψ control ($\psi(t) = K_\psi \gamma(t)$), the number of indexes in the path array between point A and B (L_1), the tether winding and unwinding velocities and the angle of attack (α) for both cycle phases. This selection of parameters was done for a range of wind speeds between $0m/s$ and $25m/s$, being the latter the defined cut-out wind speed. Table 5.2 displays the parameters selection for different wind speeds with a $0.5m/s$ step and the resultant power output. The indexes 1 and 2 refer to the production and retraction phase respectively.

For low wind speeds the reel-in and reel-out velocities had to be adjusted for a consistent motion, since it is still noticeable an oscillatory response without attenuation, as referenced in Chapter 4.2. With stronger winds, α_2 tends to increase as for larger wind speeds the required lift coefficient to maintain the kite in the air is lower. The K_ψ gain decreases with an increasing wind speed since with stronger aerodynamic forces the variation of the roll angle determines more abrupt responses in the direction control. The number of indexes (L_1) that determines the reference target point (B) has to be increased with the increment in wind speed since the kite speed also increases and for a correct adjustment of the kite direction it is necessary a further reference from A.

Figure 5.7 shows the resultant mechanical power output for different wind speeds and Figures 5.8 and 5.9 illustrate the motion of the kite for a wind speed of $7m/s$ in which is noticeable the oscillatory motion during the retraction phase.

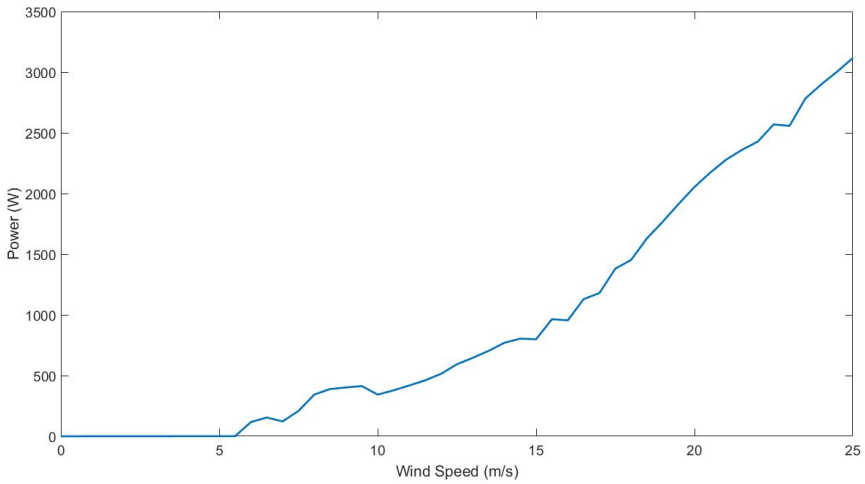

Figure 5.7: Mechanical Power Output.

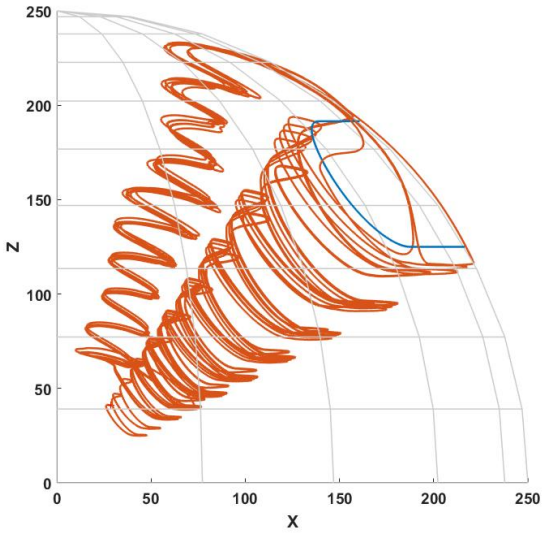

Figure 5.8: Complete Production Cycle Of A 2000s Simulation With $v_w = 7m/s$.

5.4 Power Curve, Average Power and Capacity Factor

The Mechanical Power Output found in Section 5.3 represents an output of the system without limitations. However, there are several components, such as the generator or power electronics interfaces that must be projected for a given rated power. Therefore, the power curve of the KPS must be limited, *i.e.*, a maximum power output must be defined. Figure 5.10 presents the unlimited mechanical power output and two variations with an incorporated limit. The first one describes a power curve with the average power limited to $1.5kW$ and the second one with the instantaneous power limited to $7kW$. Disregarding the power curve drawn from the unlimited system, we can develop further studies based on the curves with a limited average power output (P1) and with a limited instantaneous power (P2), as shown in figure 5.11.

The annual average power (P_{avg}) and capacity factor (c_f) can be computed through the following equations:

$$P_{avg} = \int P(v) f(v) dv \tag{5.5}$$

$$c_f = \frac{P_{avg}}{P_N}. \tag{5.6}$$

Being $f(v)$ the probability density function chosen to describe the wind speed variations and P_N the nominal power of the system. Since, the KPS we are addressing has a quasi-steady working mode with tether lengths between $70m$ and $250m$ and the average elevation angle in the production phase is 40^o, the average height of the production phase is $\frac{250+70}{2} sin(40^o) = 102.9m$. The

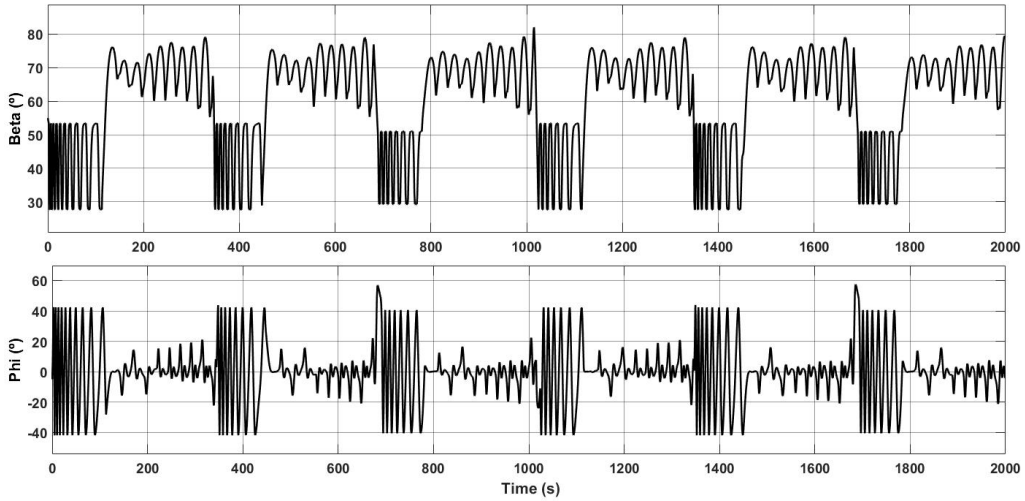

Figure 5.9: State Variables (β, ϕ) Of A 2000s Simulation In Degrees With $v_w = 7m/s$.

closest height for which GWA shows wind climate data is $100m$. Therefore, is used the Rayleigh distribution described in Subsection 5.2.2, for an altitude of $100m$. The resultant annual average power for the two considered power curves is $P_{avg1} = 444.3W$ and $P_{avg2} = 398.7W$. Considering $P_N = 1.5kW$, the consequent capacity factors are $c_{f1} = 29.62\%$ and $c_{f2} = 26.58\%$.

System parameters such as the average elevation angle or rated power influence greatly the obtained power output or capacity factors. From [30], we take the following power extraction formula that shows the impact of the chosen operation elevation angle on the power extracted from the wind.

$$P_{output} = \mathbf{v}_w F_{aer} \cos(\beta). \tag{5.7}$$

Therefore, an alteration of the average elevation angle to 30^o would cause an output power equal to $\frac{\cos(30^o)}{\cos(40^o)} = 113\%$ of the power achieved with an average elevation angle of 40^o, as used previously. The alteration of the system rated power influences directly the capacity factor and the system costs, since there are components whose cost depends on the nominal power such as the generator and power electronics devices. Hence, a balanced maximum power must not be too high, since it would result in a system that rarely functions at its nominal power and would increase its total costs, nor too low, since it would be a system which would not explore its full wind energy conversion capabilities. Figure 5.12 shows three power curves with average power output limited to $1, 1.5$ and $2kW$. The annual average power taken from these power curves is $400.0W$, $444.3W$ (P_{avg1}) and $469.9W$, respectively. There is an increase of the annual average power output with the rated power increase, as expected, but the resultant capacity factors suffer a constant decrease being 40.0%, 29.62% (c_{f1}) and 23.5%.

This chapter allows to estimate the power produced by the PKG in a certain location. The produced power depends on the technology characteristics and on the local conditions, such as the

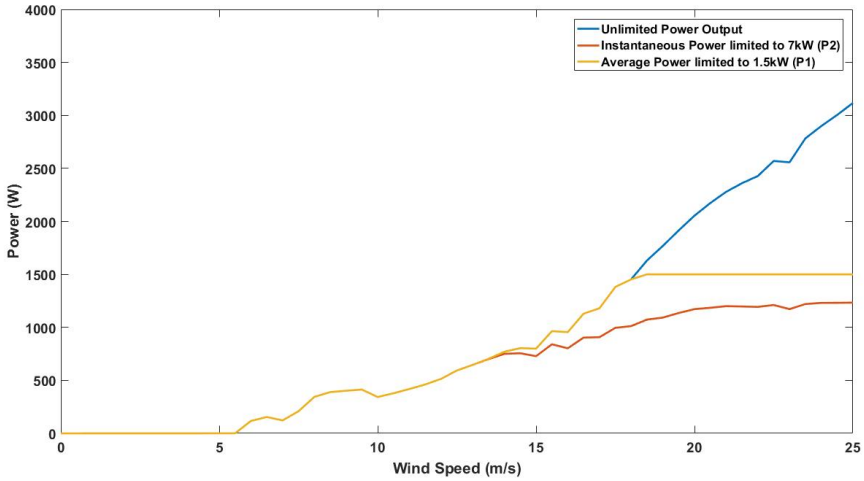

Figure 5.10: Mechanical Power Output.

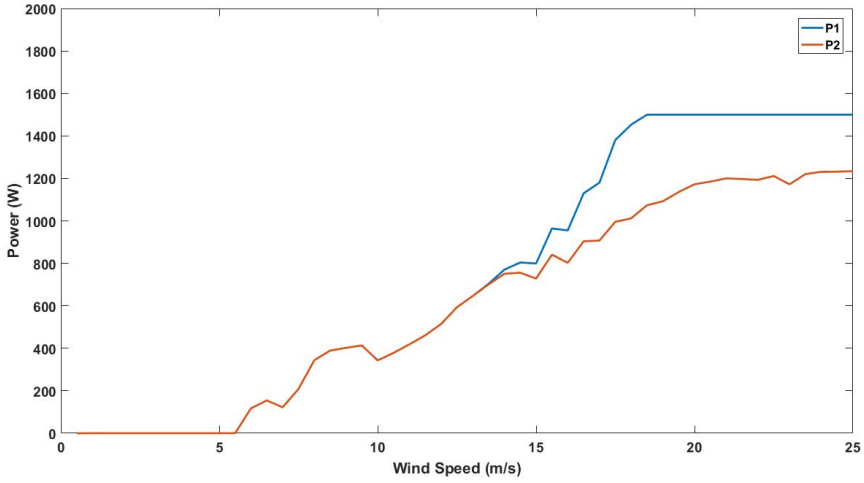

Figure 5.11: Power Curve.

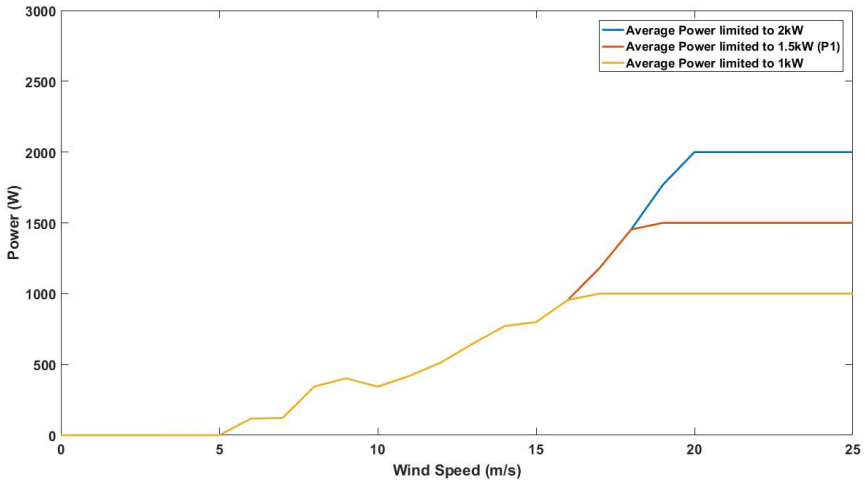

Figure 5.12: Power Curves For 1, 1.5 And 2kW Average Power Output limits.

expected wind speeds.

The value obtained for the prospected annual average power output is affected due to non-optimal parameters adjustment in the power curve construction and by the fact that the local wind representation does not consider certain wind variations, such as the variation with altitude and turbulent winds, besides not being based on actual local measurements.

The values obtained during this chapter are used in an Economical Analysis described in Chapter 6.

Table 5.2: Parameters for Energy Output Maximization

$v_w(m/s)$	$\alpha_1(^{\mathbf{o}})$	$\alpha_2(^{\mathbf{o}})$	K_ψ	L_1	$\dot{r}_1(m/s)$	$\dot{r}_2(m/s)$	$P(W)$
6	12	12.9	11	12	1.1	-0.8	117
6.5	12	13	11	12	1.15	-0.8	154
7	12	13	11	12	1.805	-0.8	122
7.5	12	13	11	14	1.805	-1.2	208
8	12	13.3	11	14	1.9	-2	344
8.5	12	13.3	11	14	2	-2	389
9	12	13.3	11	14	2.4	-2	402
9.5	12	13.3	11	14	2.7	-2	413
10	12	13.3	9	19	$v_w/3$	-2.3	343
10.5	12	13.3	8	20	$v_w/3$	-2.3	378
11	12	13.3	8	20	$v_w/3$	-2.3	418
11.5	12	13.3	8	20	$v_w/3$	-2.3	461
12	12	13.3	8	20	$v_w/3$	-2.3	514
12.5	12	13.3	8	20	$v_w/3$	-2.3	593
13	12	13.3	8	25	$v_w/3$	-2.3	646
13.5	12	13.3	8	25	$v_w/3$	-2.3	704
14	12	13.3	8	25	$v_w/3$	-2.3	770
14.5	12	13.3	8	39	$v_w/3$	-2.3	804
15	12	13.3	8	40	$v_w/3$	-2.3	799
15.5	12	13.3	8	43	$v_w/3$	-2.3	964
16	12	13.3	8	46	$v_w/3$	-2.3	955
16.5	12	13.3	8	45	$v_w/3$	-2.3	1130
17	12	13.3	8	46	$v_w/3$	-2.3	1180
17.5	12	13.3	8	46	$v_w/3$	-2.3	1381
18	12	13.3	8	46	$v_w/3$	-2.3	1453
18.5	12	13.3	8	46	$v_w/3$	-2.3	1631
19	12	13.3	8	51	$v_w/3$	-2.3	1768
19.5	12	13.3	8	51	$v_w/3$	-2.3	1914
20	12	13.3	8	51	$v_w/3$	-2.3	2054
20.5	12	13.3	8	51	$v_w/3$	-2.3	2173
21	12	13.3	8	51	$v_w/3$	-2.3	2279
21.5	12	13.3	8	51	$v_w/3$	-2.3	2360
22	12	13.3	8	51	$v_w/3$	-2.3	2428
22.5	12	13.3	8	51	$v_w/3$	-2.3	2570
23	12	13.3	8	51	$v_w/3$	-2.3	2557
23.5	12	13.3	8	51	$v_w/3$	-2.3	2783
24	12	13.3	8	51	$v_w/3$	-2.3	2899
24.5	12	13.3	8	51	$v_w/3$	-2.3	3004
25	12	13.3	8	51	$v_w/3$	-2.3	3117

Chapter 6

Economical Analysis

This chapter explores the economic performance of the PKG. Section 6.1, based on the mechanical power output found in Section 5.4, assesses the electrical annual energy production. Sections 6.2 and 6.3 list the costs of such a system throughout its lifetime and Section 6.4 concludes the Levelized Cost of Energy (LCOE) of the system in the chosen location, allowing a comparison with other technological alternatives.

6.1 Efficiency and Annual Energy Production (AEP)

The annual average power produced calculated in Chapter 5.4 corresponds to the mechanical power withdrawn from the kite power system. To estimate the electrical power, *i.e.*, the effective power output of the KPS it is necessary to take into consideration the efficiency of the components that compose the interface between the kite and the electrical grid/load, such as the winch drum, gearbox and electric generator.

In [31], a value of the electric generator (η_{EG}) and gearbox (η_{GB}) efficiency coefficients of 90% and 95%, respectively, are assumed, thus reckoning the total interface efficiency as $\eta = \eta_{EG}\eta_{GB} = 85.5\%$. Consequently, the electrical/effective mean annual power outputs are $P_{avg1.elec} = 379.8W$ and $P_{avg2.elec} = 340.9W$.

Multiplying the mean annual power by 8760 (number of hours in a year), we find the Annual Energy Produced (AEP) being $AEP1 = 3.33MWh$ and $AEP2 = 2.99MWh$ for each power output characteristic.

6.2 Initial Capital Cost (ICC)

To estimate the Initial Capital Cost (ICC) it is required to list several components for the system assembly and its costs.

6.2.1 Aircraft and Tether

The aircraft in which simulation characteristics were based is a Multiplex Easystar II model airplane. As stated in previous chapters, it has a wing area of $0.28m^2$ and a total weight of $0.7kg$. This model can be found from $80-150$€, but for the purpose of this calculation it will be defined a cost of 200€per aircraft.

The tether main defining characteristics are its weight, diameter and the force it can withstand. For a $25m/s$ wind velocity (cut-out wind speed) the maximum instantaneous tether force obtained from the simulations reaches a value of $10.3kN$ ($1052kg$). Based on Samson Industrial Catalog [32], a Dyneema rope with a $4mm$ diameter has an average strength of $1800kg$, 1.7 times the maximum force that the tether would have to sustain. The price of such a line stands in $0.18€/m$, thus, defining a total length of $350m$, it would be of 63€.

6.2.2 Electric Power Generation and Interface Components

In [33] cost functions for different parts of component groups are stated depending on its respective requirements. For the Mechanical Power Conversion group, which combines the winch drum, electric generator and gearbox, the cost function depends on the Nominal Power of the system and Nominal Force as described by the succeeding equation.

$$C_{\text{mech.power conv.}} = 100 P_N^{\frac{1}{2}} F^{\frac{3}{4}}. \tag{6.1}$$

Considering a nominal power of $1kW$ and the maximum force of $10.3kN$ as the nominal force, the estimated cost of the Mechanical Power Conversion components is 575€. The value chosen for the nominal force is oversized for the system which will cause an overpricing of certain components.

The cost of the Electrical Power Conversion components, such as inverter, transformer and storage elements, and the cost of transport and installation of the KPS unit are set as linear functions of the nominal power, being the latter 150 and the former 100 times the value of the systems power [33]. Therefore, the aggregate cost of both these parts sets on 250€.

6.2.3 Other Components

A walk through and cost breakdown of a small-scale KPS prototype without energy generation capabilities, described in [34], is followed to base the cost estimation of the remaining components.

The system described in this paper relies on a Leading Edge Inflatable (LEI) kite controlled by three tethers, diverging from the proposed in this dissertation. Therefore, the direction controllers are built outside the aircraft, which allows for some components listed, such as Linear Motion Systems (LMS), electric motors and drives for steering and wing pitch control, to be disregarded.

For the appraisal of the control hardware cost, we considered the cost function, present in [35] and presented below, for the Kite Control Unit (KCU). Although the control unit for the described PKG differs from the system assessed in this dissertation.

$$C_{\text{KCU}} = 100F + 2500. \tag{6.2}$$

Since we have been considering the maximum force of $10.3kN$, the cost of the control unit is 3530€.

Table 6.1 displays the final cost estimation of the complete system. The costs expressed in US dollars in the referenced texts were converted at a conversion rate of 1$=0,86€.

Table 6.1: Cost Breakdown of System Components

Component	**Cost(€)**
Control hardware	3530
Mechanical Frame	2838
Consumables (wiring, connectors, etc.)	2150
Kite	200
Tether	63
Mechanical Power Conversion components	575
Electrical Power Conversion components	100
Transport and Installation	150
Total	**9606**

6.3 Operation and Maintenance (O&M) and Replacement Costs

Considering a lifetime of 20 years and the replacement of the kite, tether, gearbox and electric generator every 5 years, since these are components that must uphold strong and inherently periodic mechanical and/or electrical efforts, we compute the present value of the necessary replacement costs through:

$$C_0 = \sum \frac{C}{(1+i)^t} \tag{6.3}$$

In which i is the fixed discount rate and t is the year in which a cash flow (C) takes place. For $i = 10\%$ the resultant present value of the considered replacements is 1044€.

Data from European Wind Energy Association, [36], determines that Operation and Maintenance (O&M) costs reach $20-25\%$ of the total costs of a wind turbine over its lifetime. Admitting a value of 25% for this KPS, O&M would set on 3550€.

6.4 Levelized Cost of Energy (LCOE)

The Levelized Cost of Energy (LCOE) is a method of comparing technologies without taking into consideration the remuneration, since the income varies with the local energetic policies, such as feed-in tariffs and local market circumstances. It can be calculated through the equation (6.4) in which both cash (C) and energy flows (E) are actualized.

$$LCOE = \frac{\sum_t \frac{C}{(1+i)^t}}{\sum_t \frac{E}{(1+i)^t}}. \tag{6.4}$$

For the system in question, the LCOE, for a 20 years lifetime, would be 448€$/MWh$ for $AEP1$ and 499€$/MWh$ for $AEP2$. These values, compared to other estimates and technologies, are quite high. This could be a consequence of a non-optimal power output, due to the flawed control variables choice during the power curve construction, and of a overrated pricing during the cost estimation, caused by oversized parameters such as a nominal force of 10.3kN.

[33] explores the influence of main system and site parameters on the resultant LCOE of large KPS. System parameters such as the kite area or rated power affect directly the cost of a system and the capacity factor, thus it is required a balance between these characteristics to find a cost-effective solution. [33] reaches a variation of LCOE of 40-110€$/MWh$, varying the annual average wind speed from 4m/s to 10m/s and demonstrating the impact of site conditions on the production and consequently on the cost of energy. A comparative cost analysis for a 2MW system in [37] reaches costs between 10-50\$$/MWh$ and, regarding the possibility of kite wind farms, [38] predicts LCOE values between 20-50\$$/MWh$, depending on the farm size. Table 6.2 shows the LCOE forecasts for different PKG taken from a 2018 European Commission report[39].

Table 6.2: LCOE Forecasts [39]

Source of Estimate	**LCOE (€/MWh)**	**year**	**Additional Information**
Ampyx	120	not defined	for 2MW unit, floating offshore
EnerKite	85	2019	for 100kW unit
Enerkite	46	2020	for 500kW unit
Kitepower/Enevate	150	2018	for 100kW unit
Kitepower/Enevate	105	not defined	for 100kW unit and 250 m^2 wing area
Kite Power Systems	100	2022	
Skypull	40.2	not defined	
Fraunhofer IWES	46	not defined	for 200kW unit
Politecnico di Torino	10 to 48	not defined	for large farms of 2MW units
P. Faggiani and R. Schmehl	125	not defined	for a flexible wing, 100kW unit and 100m^2 wing area

Chapter 7

Wind Farm Ground Area Usage

A single KPS unit requires large batteries to deliver a stable electrical output due to its highly variable nature, since it generates and consumes electricity cyclically. Several units organized in a wind farm can be a solution to guarantee a continuous output with low storage requirements.

The Wind Farm possibility raises a few issues, such as the spacing of KPS units, developed in Section 7.1, and the synchronization of parts of the wind farm in order to balance the total net output, analyzed in Section 7.2.

7.1 Spacing of KPS Units

To optimize the ground area usage of a wind farm, the distance between units needs to be the minimum distance in which the units do not affect each others operation. In conventional wind parks, the spacing of wind turbines is usually defined to avoid wake effects. But the wake effect is negligible in kite wind farms, due to the relatively small wing surface area and because different kites can be working with different altitudes and alignment. However, the spacing of units in a kite wind farm is an important issue because of the possibility of entangled tethers or even kite collision. The definition of the flight envelope must avoid mechanical interaction between units [40].

The fact that each unit aligns with the wind direction has to be considered when defining the minimum distance between them. Therefore, we will explore two distinct possibilities in which the most restrictive will define the distance between KPSs. One in which two units are working in parallel and one in which the units are aligned. In the first case, represented in Figure 7.1, the minimum distance between units (d) can be simply calculated through equation (7.1), as in [40]

$$d = 2r_{\max}\sin(\Delta\phi). \tag{7.1}$$

Where r_{max} is the maximum tether length and $\Delta\phi$ is the maximum deviation of ϕ from the center during the production phase.

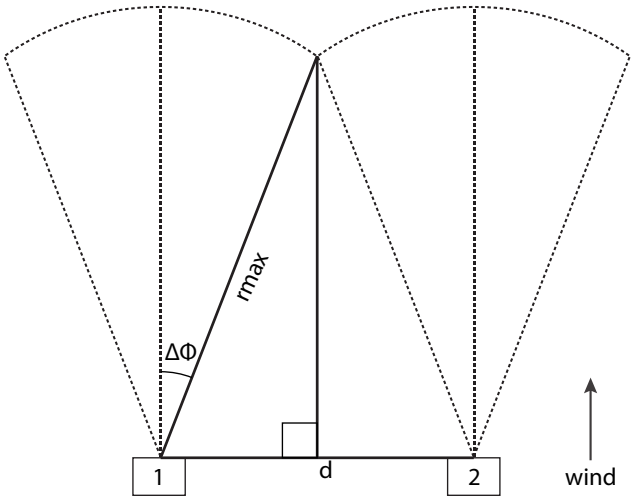

Figure 7.1: Minimum Distance Between Parallel Kites.

In the second case, the minimum distance between units can be calculated decomposing the triangle that unites both ground stations and the point in which the flight envelopes can intersect in two right triangles, as presented in Figure 7.2. The line dividing the two right triangles has a length equal to $\frac{r_{max}}{\frac{1}{tan(\beta_0-\Delta\beta)}+\frac{1}{tan(2\Delta\beta)}}$ and equal to $dsin(\beta_0-\Delta\beta)$ as well [40]. Therefore, the minimum distance between units when these are aligned is:

$$d = \frac{r_{max}}{sin(\beta_0-\Delta\beta)\left(\frac{1}{tan(\beta_0-\Delta\beta)}+\frac{1}{tan(2\Delta\beta)}\right)}. \tag{7.2}$$

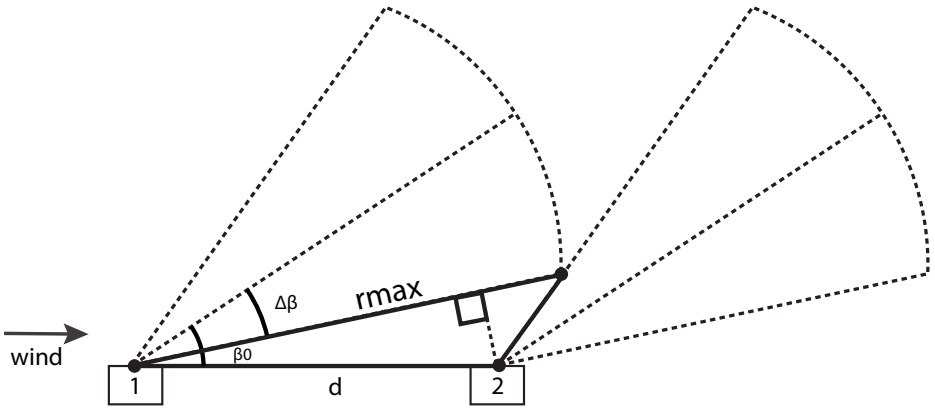

Figure 7.2: Minimum Distance Between Aligned Kites.

This calculation considers that aligned kites must work synchronized, *i.e.*, must be in the same phase of the generation cycle, otherwise this spacing would be insufficient.

Using the parameters set for the single unit simulations in the previous chapters, the most restricting, thus the defining, distance would be the one in which the units are in parallel and $d = 250m$, since for aligned kites the minimum distance would be of $111.6m$.

7.2 Electrical Output

Aiming to guarantee a stable electric output of a wind farm, the units must operate with a certain phase shift, *i.e.* kites should not be operating in the same production/retraction phase at the same time to avoid production and consumption peaks.

Considering a squared *n*x*n* wind farm, there are two extreme possibilities of alignment. One in which the wind direction is orthogonal to a wind farm side and one in which the wind is aligned with the diagonal of the squared arrangement. Since aligned units must work concurrently, the alignment defines columns of synchronized units, that serve as the basis for the phase shifts setting.

For the case of the wind direction orthogonal to the square side, the number of columns would be n with n units in each column and in the case of a diagonal wind there would be $2n-1$ columns in which one consists in n units and the remaining columns would have $n-1, n-2, ..., 2, 1$ units with two columns for each number of units.

In [40], the phase shifts for the first case are established as the cycle duration (T) divided by the number of columns (n) and for the case of a diagonal wind, the phase shifts are calculated as the double of the cycle duration divided by the number of columns $\left(\frac{2T}{2n-1}\right)$. The resultant power output shows that orthogonal winds display a more constant power and that diagonal winds result in periodic large oscillations.

However, a simple phase shift configuration, as in Figure 7.3, might allow an equal power output for both cases in which the phase shift will be set as $\frac{T}{n}$. The arrangement for orthogonal winds is the same as proposed in [40], but for diagonal winds the inner columns (*e.g.* a column with $n-1$ kites) could be matched with an outer column (a column with 1 unit) thus defining n sets of n kites for each phase. Figure 7.3 shows a wind farm with 4x4 KPS for both orthogonal and diagonal winds, the columns with the same shift display the same color.

For a squared wind farm, such as the one presented in Figure 7.3, with KPS units based on the characteristics set in previous chapters, taking into consideration a wind velocity of $10m/s$, a full production cycle with the reeling velocities of $v_w/3m/s$ for the production phase and $-2m/s$ for the retraction phase, lasts $128s$, hence the phase shift would be of $32s$. Figure 7.4 shows overlapped trajectories of divergent phases for a $1h$ simulation.

Figure 7.5 shows that the wind farm energy output is smoother than a single kite system benefiting the final electrical output and allowing a reduced per unit electrical storage capacity for a continuous operation. Therefore, the exploration of KPS in a wind farm configuration can cause lower LCOE values per unit due to cost reduction. Figure 7.6 shows an asymptotic variation of LCOE with the number of units in a wind farm, taken from [40].

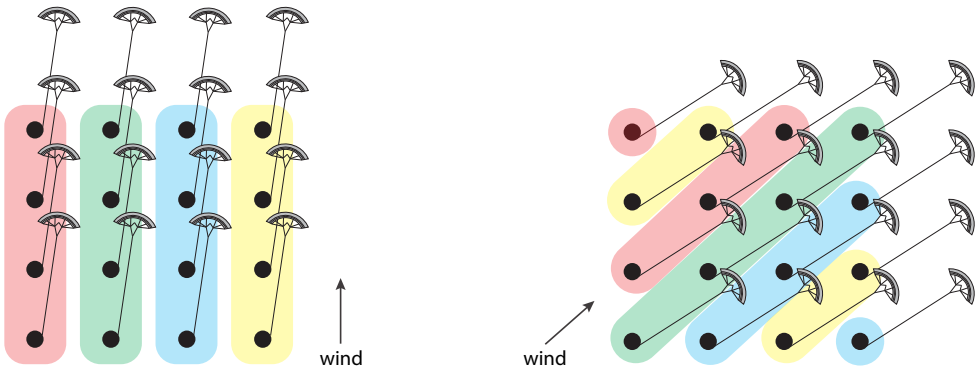

Figure 7.3: Kites Orientation And Phase Shifts.

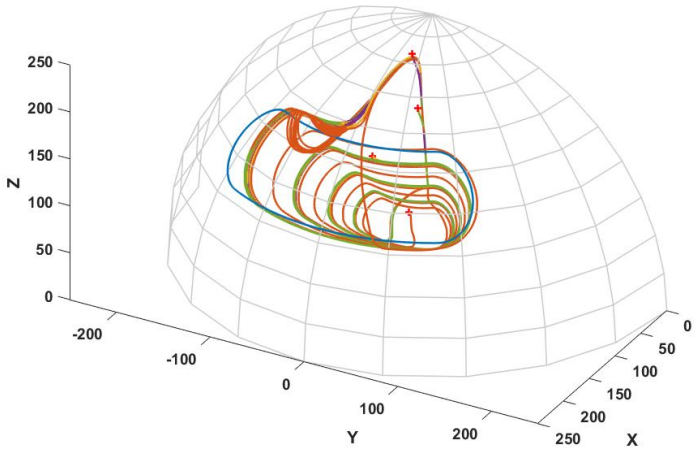

Figure 7.4: Overlapped Trajectories Of Different Phase Shifts.

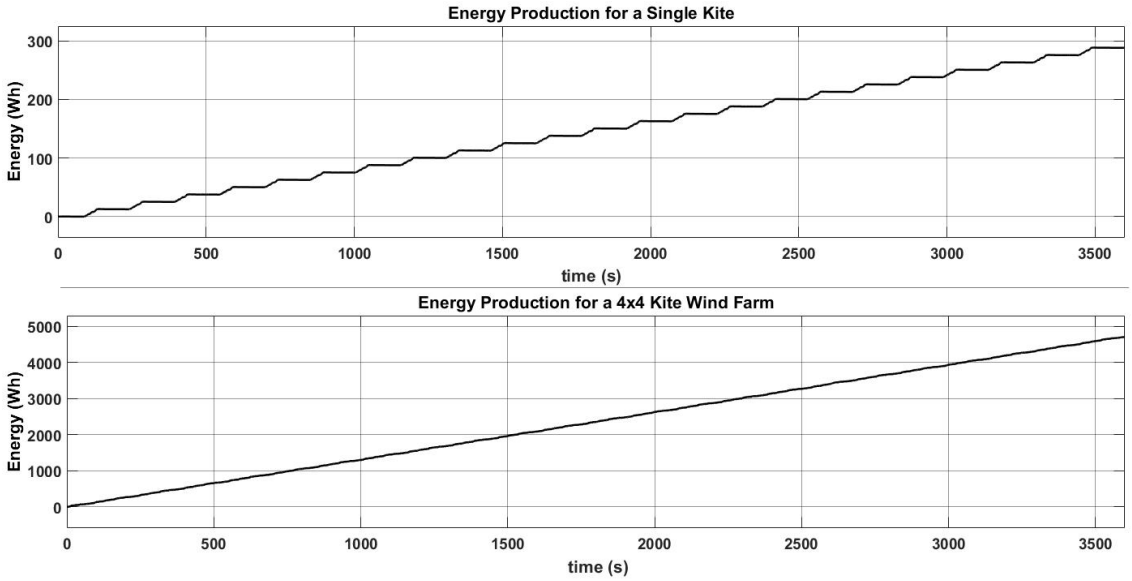

Figure 7.5: Energy Production Of A Single KPS Unit And A 4x4 Wind Farm.

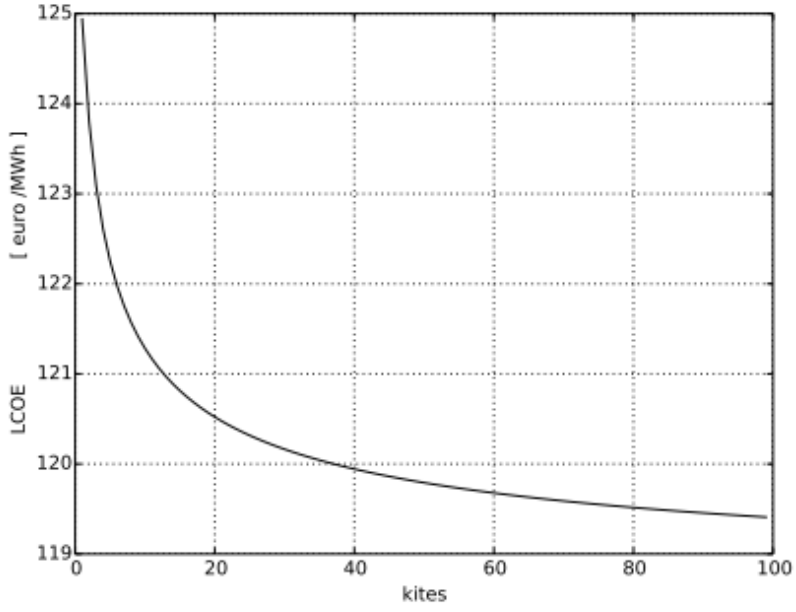

Figure 7.6: LCOE Variation With The Number Of Units In A Wind Farm [40].

Chapter 8

Conclusions and Future Work

Dynamic simulation models of a KPS, based on a mass-point description of the airfoil, and analysis of different perspectives of its motion and responsive behaviour are developed. In a 2D model of its dynamics, it is evaluated the response to different wind speeds and angles of attack of the kite and the impact of the $c_L(\alpha)$ and $c_D(\alpha)$ coefficients in the elevation and aerodynamic forces. It is noticeable, for the proposed system characteristics, an oscillatory motion for low wind speeds due to a low drag. The point in which the lift force equals the weight of the system defines the elevation wind speed for a given angle of attack and allows us to estimate the proper α to control the kite during extreme wind conditions.

In a 3D model, a method to control the kite trajectory is developed. A desired path, set only on ϕ and β permits an adjustable steering reference regarding the tether length and winding velocity. The trajectory controller for the production phase is based on the variation of ψ with a constant α, since the adjustment of the roll angle is an adjustment of the lift force direction and consequently the kite direction. In the case of wind gusts, the angle of attack plays an important role in limiting the aerodynamic forces in such a way that the resultant tether tension does not jeopardize the system components.

The control variables for varying wind speeds are defined to reach a power curve, that permits the assessment of the system implementation possibility and economical evaluation for a given site. Based on the power curve and the wind speed probability density function, it is estimated the average power and energy output throughout a year. The prospected production and a cost estimation of the system are used in order to calculate the Levelized Cost of Energy (LCOE) which allows an economical comparison of the PKG to other technologies or similar systems.

For a possible exploration of a wind farm, the minimum spacing between KPS units is studied for the possibility of aligned and parallel kites. For a squared wind farm, it is determined the phase shift between groups of synchronized/aligned kites for wind directions orthogonal and diagonal to the wind farm, being proposed a strategy to guarantee a smooth aggregate electrical output of the farm.

For future development, the Matlab/Simulink models can be altered to test and evaluate PKG systems with different characteristics and different control mechanisms in order to ameliorate the

system response. Through this tool, a comparative analysis between kites or airfoils could be developed, aiming to assess the best configuration for a physical prototype or its adequacy to a given location or conditions. In order to approach a more realistic simulation model, parameters such as tether weight and drag and wind variations, such as wind shear and high frequency wind speed variations, can be added. The incorporation of these parameters could also be used to determine optimal tether length and operation altitude.

Appendix A

Auxiliary Equations

The and equations for the 2D and 3D model are derived in this chapter.

A.1 2D Model

$$\mathbf{p} = \begin{bmatrix} r\cos(\beta) \\ r\sin(\beta) \end{bmatrix} \tag{A.1}$$

$$\begin{aligned}
\dot{\mathbf{p}} &= \frac{d\mathbf{p}}{dt} && \text{(A.2)} \\
&= \frac{\partial \mathbf{p}}{\partial r}\frac{dr}{dt} + \frac{\partial \mathbf{p}}{\partial \beta}\frac{d\beta}{dt} && \text{(A.3)} \\
&= \frac{\partial \mathbf{p}}{\partial r}\dot{r} + \frac{\partial \mathbf{p}}{\partial \beta}\dot{\beta} && \text{(A.4)} \\
&= \begin{bmatrix} \cos(\beta) \\ \sin(\beta) \end{bmatrix}\dot{r} + \begin{bmatrix} -r\sin(\beta) \\ r\cos(\beta) \end{bmatrix}\dot{\beta} && \text{(A.5)} \\
&= \dot{r}\vec{\mathbf{e}}_r + r\dot{\beta}\vec{\mathbf{e}}_\beta && \text{(A.6)} \\
&= \begin{bmatrix} \dot{r} \\ r\dot{\beta} \end{bmatrix}_{\mathrm{L}} && \text{(A.7)}
\end{aligned}$$

$$\ddot{\mathbf{p}} = \frac{d^2\mathbf{p}}{dt^2} = \frac{d}{dt}\left(\frac{d\mathbf{p}}{dt}\right) \tag{A.8}$$

$$= \frac{d}{dt}\left(\frac{\partial \mathbf{p}}{\partial r}\dot{r} + \frac{\partial \mathbf{p}}{\partial \beta}\dot{\beta}\right) \tag{A.9}$$

$$= \frac{\partial \mathbf{p}}{\partial r}\ddot{r} + \frac{\partial \mathbf{p}}{\partial \beta}\ddot{\beta} + \frac{\partial^2 \mathbf{p}}{\partial r^2}\dot{r}^2 + \frac{\partial^2 \mathbf{p}}{\partial \beta^2}\dot{\beta}^2 + 2\frac{\partial^2 \mathbf{p}}{\partial \beta}\dot{r}\dot{\beta} \tag{A.10}$$

$$= \begin{bmatrix}\cos(\beta)\\ \sin(\beta)\end{bmatrix}\ddot{r} + \begin{bmatrix}-r\sin(\beta)\\ r\cos(\beta)\end{bmatrix}\ddot{\beta} + \begin{bmatrix}0\\ 0\end{bmatrix}\dot{r}^2 + \begin{bmatrix}-r\cos(\beta)\\ -r\sin(\beta)\end{bmatrix}\dot{\beta}^2 + \begin{bmatrix}-\sin(\beta)\\ \cos(\beta)\end{bmatrix}2\dot{r}\dot{\beta} \tag{A.11}$$

$$= (\ddot{r} - r\dot{\beta}^2)\vec{\mathbf{e}}_r + (r\ddot{\beta} + 2\dot{r}\dot{\beta})\vec{\mathbf{e}}_\beta \tag{A.12}$$

$$= \begin{bmatrix}\ddot{r} - r\dot{\beta}^2\\ r\ddot{\beta} + 2\dot{r}\dot{\beta}\end{bmatrix}_{\mathrm{L}} \tag{A.13}$$

$$= \begin{bmatrix}\ddot{r}\\ r\ddot{\beta}\end{bmatrix}_{\mathrm{L}} + \underbrace{\begin{bmatrix}-r\dot{\beta}^2\\ 2\dot{r}\dot{\beta}\end{bmatrix}_{\mathrm{L}}}_{-\frac{1}{m}\vec{\mathrm{F}}^{\mathrm{inert}}} \tag{A.14}$$

A.2 3D Model

$$\mathbf{p} = \begin{bmatrix}r\cos(\beta)\cos(\phi)\\ r\cos(\beta)\sin(\phi)\\ r\sin(\beta)\end{bmatrix} \tag{A.15}$$

$$\dot{\mathbf{p}} = \frac{d\mathbf{p}}{dt} \tag{A.16}$$

$$= \frac{\partial \mathbf{p}}{\partial r}\frac{dr}{dt} + \frac{\partial \mathbf{p}}{\partial \phi}\frac{d\phi}{dt} + \frac{\partial \mathbf{p}}{\partial \beta}\frac{d\beta}{dt} \tag{A.17}$$

$$= \frac{\partial \mathbf{p}}{\partial r}\dot{r} + \frac{\partial \mathbf{p}}{\partial \phi}\dot{\phi} + \frac{\partial \mathbf{p}}{\partial \beta}\dot{\beta} \tag{A.18}$$

$$= \begin{bmatrix}\cos(\beta)\cos(\phi)\\ \cos(\beta)\sin(\phi)\\ \sin(\beta)\end{bmatrix}\dot{r} + \begin{bmatrix}-r\cos(\beta)\sin(\phi)\\ r\cos(\beta)\cos(\phi)\\ 0\end{bmatrix}\dot{\phi} + \begin{bmatrix}-r\sin(\beta)\cos(\phi)\\ -r\sin(\beta)\sin(\phi)\\ r\cos(\beta)\end{bmatrix}\dot{\beta} \tag{A.19}$$

$$= \dot{r}\vec{\mathbf{e}}_r + r\dot{\phi}\cos(\beta)\vec{\mathbf{e}}_\phi + r\dot{\beta}\vec{\mathbf{e}}_\beta \tag{A.20}$$

$$= \begin{bmatrix}\dot{r}\\ r\dot{\phi}\cos(\beta)\\ r\dot{\beta}\end{bmatrix}_{\mathrm{L}} \tag{A.21}$$

$$\ddot{\mathbf{p}} = \frac{d^2\mathbf{p}}{dt^2} = \frac{d}{dt}\left(\frac{d\mathbf{p}}{dt}\right) \tag{A.22}$$

$$= \frac{d}{dt}\left(\frac{\partial \mathbf{p}}{\partial r}\dot{r} + \frac{\partial \mathbf{p}}{\partial \phi}\dot{\phi} + \frac{\partial \mathbf{p}}{\partial \beta}\dot{\beta}\right) \tag{A.23}$$

$$= \frac{\partial \mathbf{p}}{\partial r}\ddot{r} + \frac{\partial \mathbf{p}}{\partial \phi}\ddot{\phi} + \frac{\partial \mathbf{p}}{\partial \beta}\ddot{\beta} + \frac{\partial^2 \mathbf{p}}{\partial r^2}\dot{r^2} + \frac{\partial^2 \mathbf{p}}{\partial \phi^2}\dot{\phi^2} + \frac{\partial^2 \mathbf{p}}{\partial \beta^2}\dot{\beta^2} \tag{A.24}$$

$$+ 2\frac{\partial^2 \mathbf{p}}{\partial r \partial \phi}\dot{r}\dot{\phi} + 2\frac{\partial^2 \mathbf{p}}{\partial \phi \partial \beta}\dot{\phi}\dot{\beta} + 2\frac{\partial^2 \mathbf{p}}{\partial \beta \partial r}\dot{\beta}\dot{r} \tag{A.25}$$

$$= \begin{bmatrix} \cos(\beta)\cos(\phi) \\ \cos(\beta)\sin(\phi) \\ \sin(\beta) \end{bmatrix} \ddot{r} + \begin{bmatrix} -r\cos(\beta)\sin(\phi) \\ r\cos(\beta)\cos(\phi) \\ 0 \end{bmatrix} \ddot{\phi} + \begin{bmatrix} -r\sin(\beta)\cos(\phi) \\ -r\sin(\beta)\sin(\phi) \\ r\cos(\beta) \end{bmatrix} \ddot{\beta} + \begin{bmatrix} 0 \\ 0 \\ 0 \end{bmatrix} \dot{r^2} \tag{A.26}$$

$$+ \begin{bmatrix} -r\cos(\beta)\cos(\phi) \\ -r\cos(\beta)\sin(\phi) \\ 0 \end{bmatrix} \dot{\phi^2} + \begin{bmatrix} -r\cos(\beta)\cos(\phi) \\ -r\cos(\beta)\sin(\phi) \\ -r\sin(\beta) \end{bmatrix} \dot{\beta^2} + \begin{bmatrix} -\cos(\beta)\sin(\phi) \\ \cos(\beta)\cos(\phi) \\ 0 \end{bmatrix} 2\dot{r}\dot{\phi} \tag{A.27}$$

$$+ \begin{bmatrix} r\sin(\beta)\sin(\phi) \\ -r\sin(\beta)\cos(\phi) \\ 0 \end{bmatrix} 2\dot{\phi}\dot{\beta} + \begin{bmatrix} -\sin(\beta)\cos(\phi) \\ \sin(\beta)\sin(\phi) \\ \cos(\beta) \end{bmatrix} 2\dot{\beta}\dot{r} \tag{A.28}$$

$$= \begin{bmatrix} \ddot{r} - r\dot{\beta^2} - r\dot{\phi^2}(1 - sin^2(\beta)) \\ r\ddot{\phi}\cos(\beta) + 2\dot{r}\dot{\phi}\cos(\beta) - 2r\dot{\phi}\dot{\beta}\sin(\beta) \\ r\ddot{\beta} + 2\dot{r}\dot{\beta} + r\dot{\phi^2}\cos(\beta)\sin(\beta) \end{bmatrix}_{\mathrm{L}} \tag{A.29}$$

$$= \begin{bmatrix} \ddot{r} - r\dot{\beta^2} - r\dot{\phi^2}\cos^2(\beta) \\ r\ddot{\phi}\cos(\beta) + 2\dot{r}\dot{\phi}\cos(\beta) - 2r\dot{\phi}\dot{\beta}\sin(\beta) \\ r\ddot{\beta} + 2\dot{r}\dot{\beta} + r\dot{\phi^2}\cos(\beta)\sin(\beta) \end{bmatrix}_{\mathrm{L}} \tag{A.30}$$

$$= \begin{bmatrix} \ddot{r} \\ r\ddot{\phi}\cos(\beta) \\ r\ddot{\beta} \end{bmatrix}_{\mathrm{L}} + \underbrace{\begin{bmatrix} -r\dot{\beta}^2 - r\dot{\phi}^2\cos^2(\beta) \\ 2\dot{r}\dot{\phi}\cos(\beta) - 2r\dot{\phi}\dot{\beta}\sin(\beta) \\ 2\dot{r}\dot{\beta} + r\dot{\phi}^2\cos(\beta)\sin(\beta) \end{bmatrix}_{\mathrm{L}}}_{-\frac{1}{m}\vec{\mathrm{F}}^{\mathrm{inert}}} \tag{A.31}$$

Appendix B

3D Matlab/Simulink Model Subsystems

This chapter holds figures of the 3D Matlab/Simulink Model Subsytems.

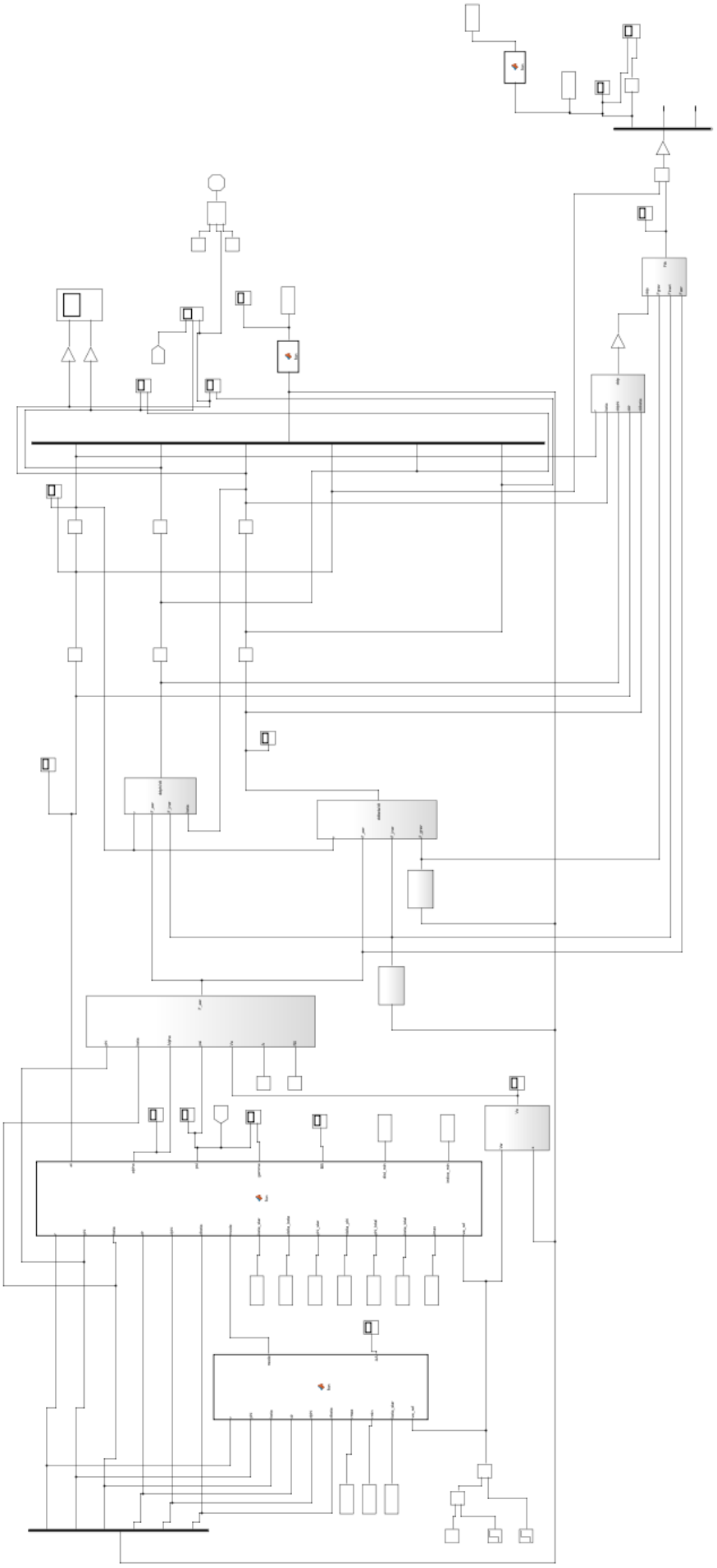

Figure B.1: 3D Matlab/Simulink Model.

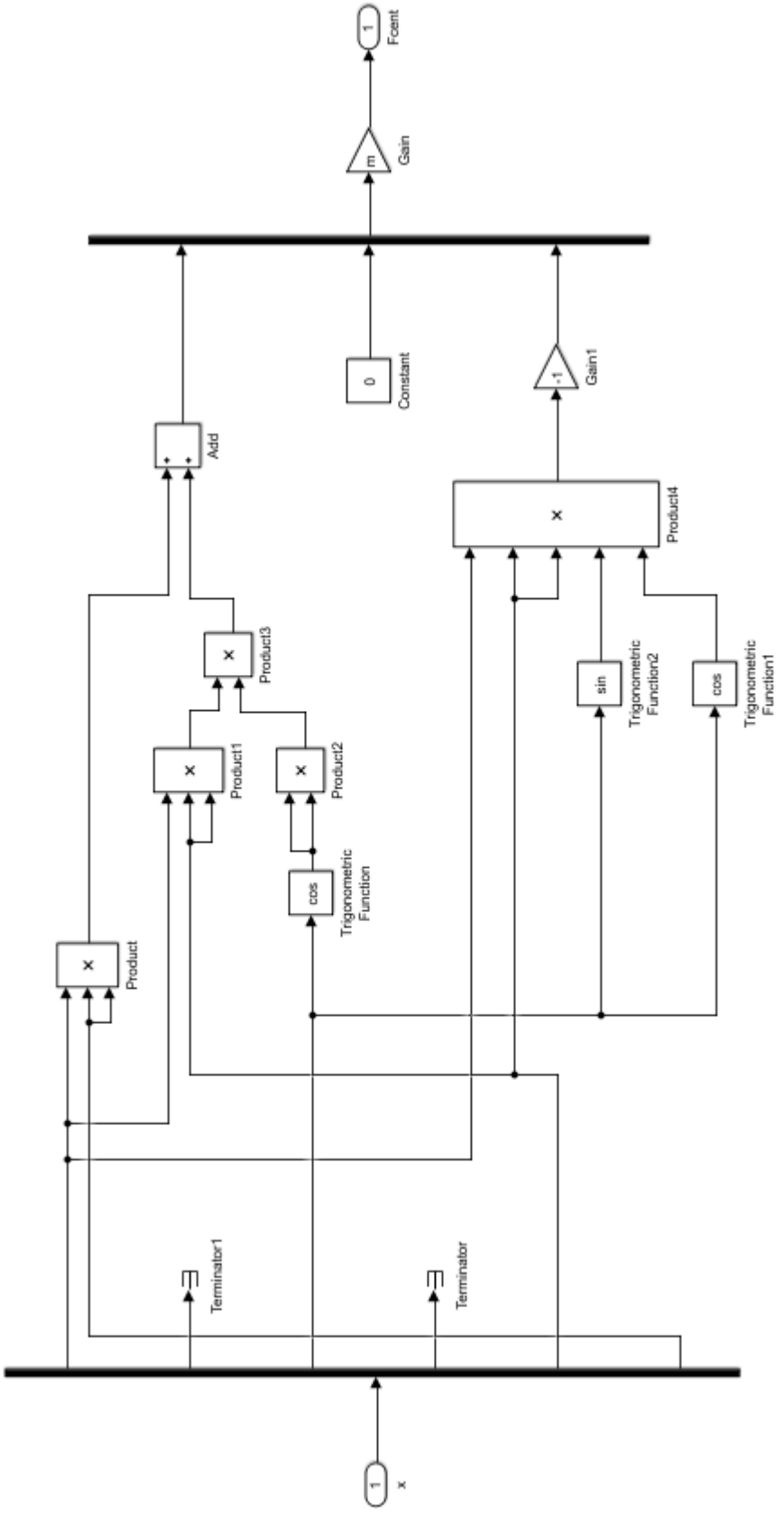

Figure B.2: Centrifugal Force Subsystem.

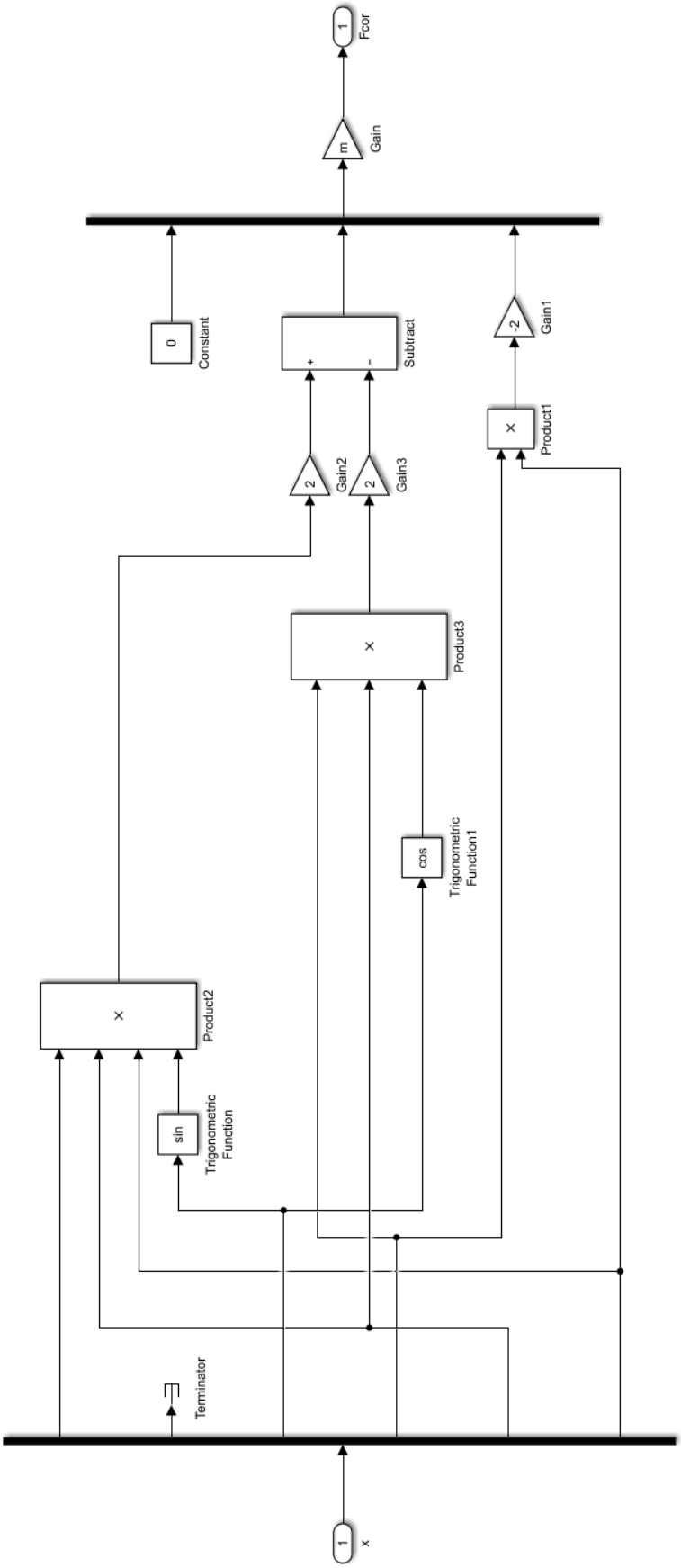

Figure B.3: Coriolis Force Subsystem.

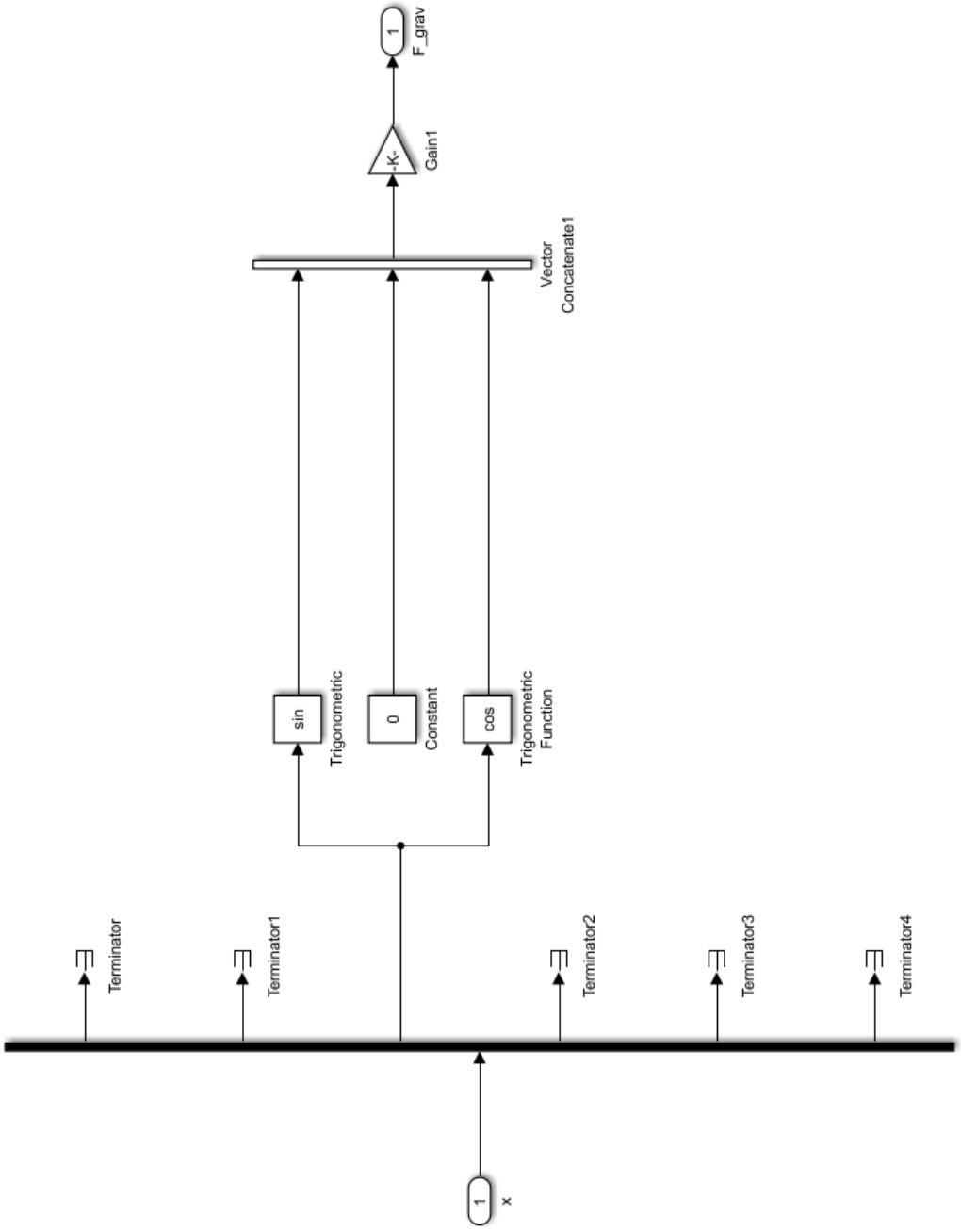

Figure B.4: Force of Gravity Subsystem.

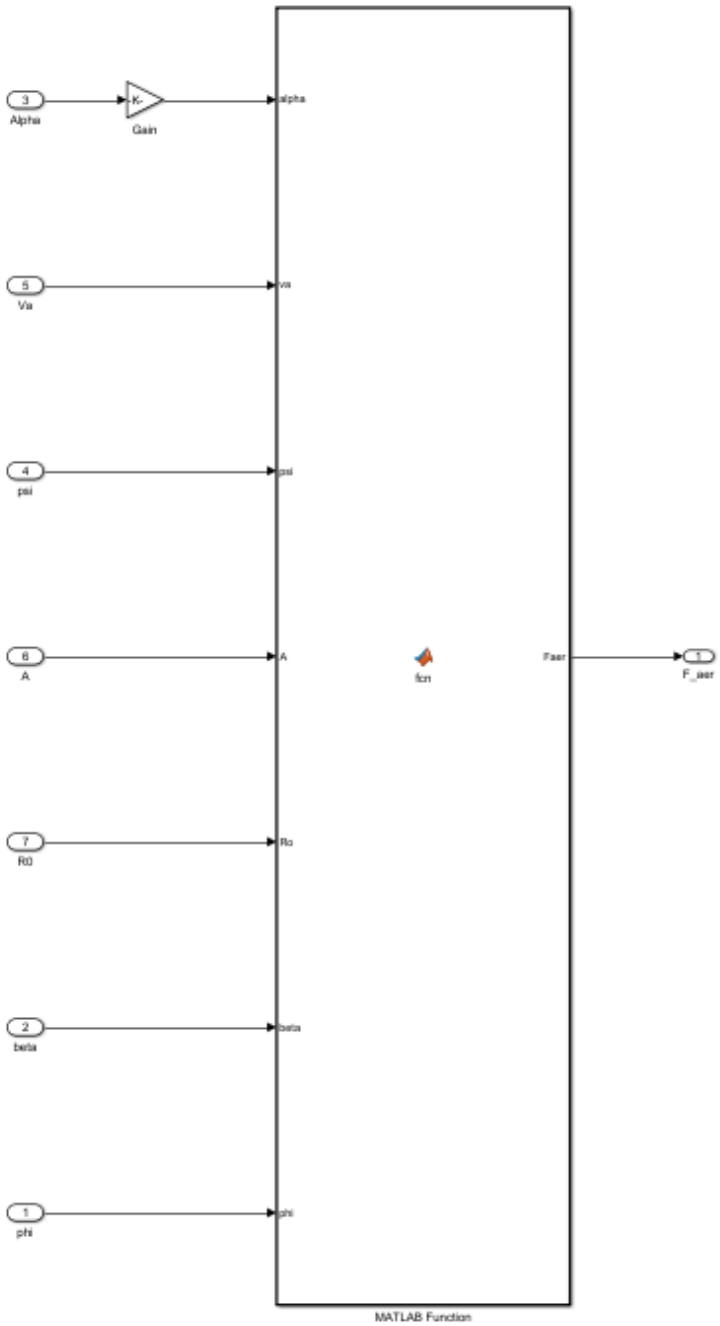

Figure B.5: Aerodynamic Forces Subsystem.

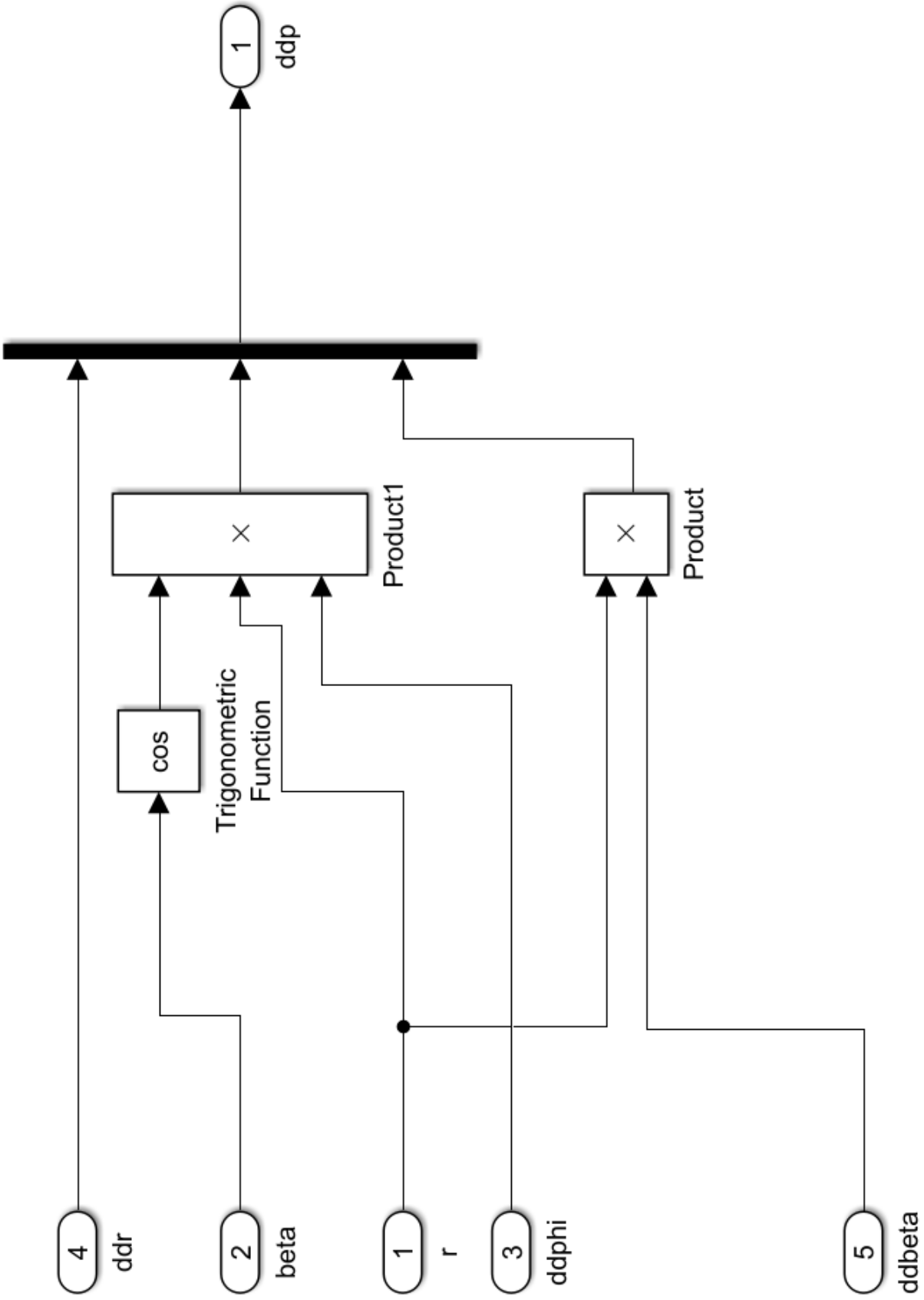

Figure B.6: $\ddot{\mathbf{p}}$ Subsystem.

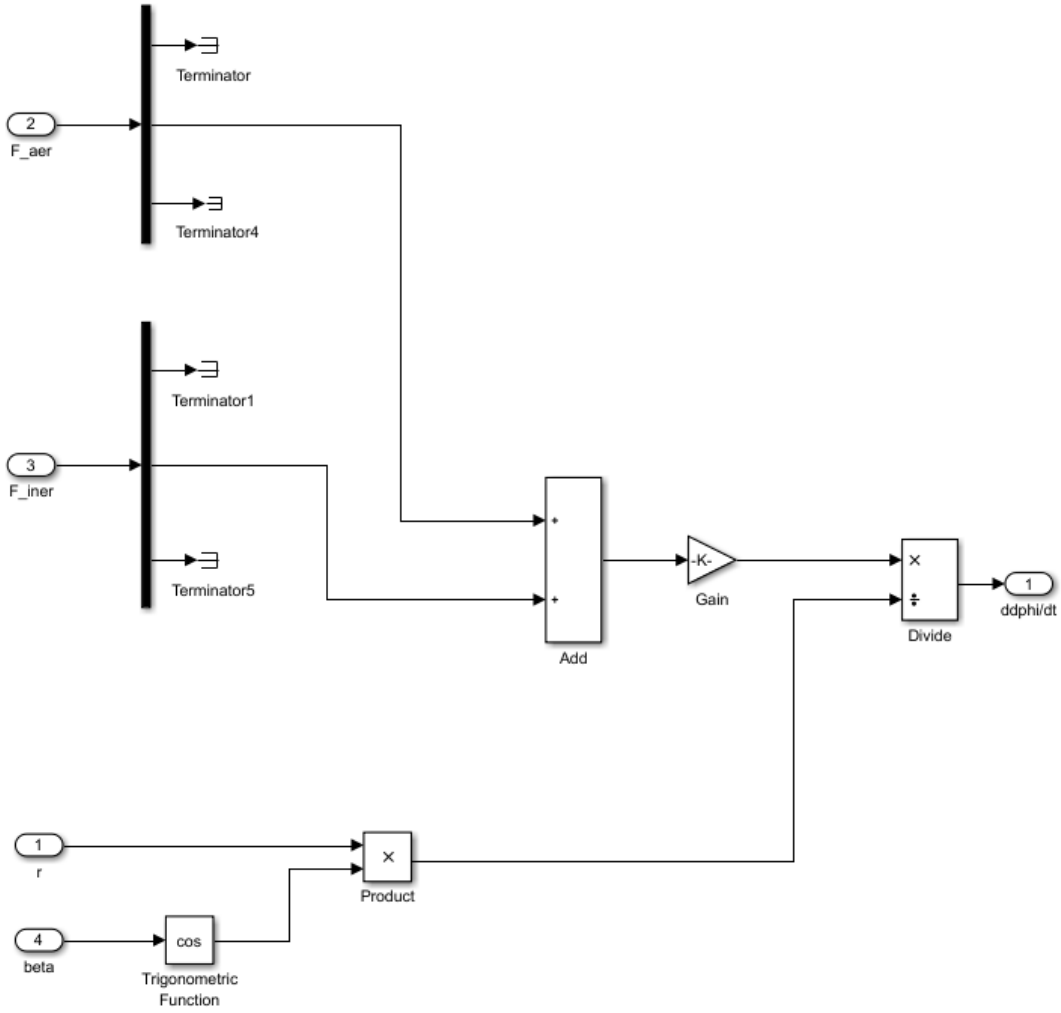

Figure B.7: $\ddot{\phi}$ Subsystem.

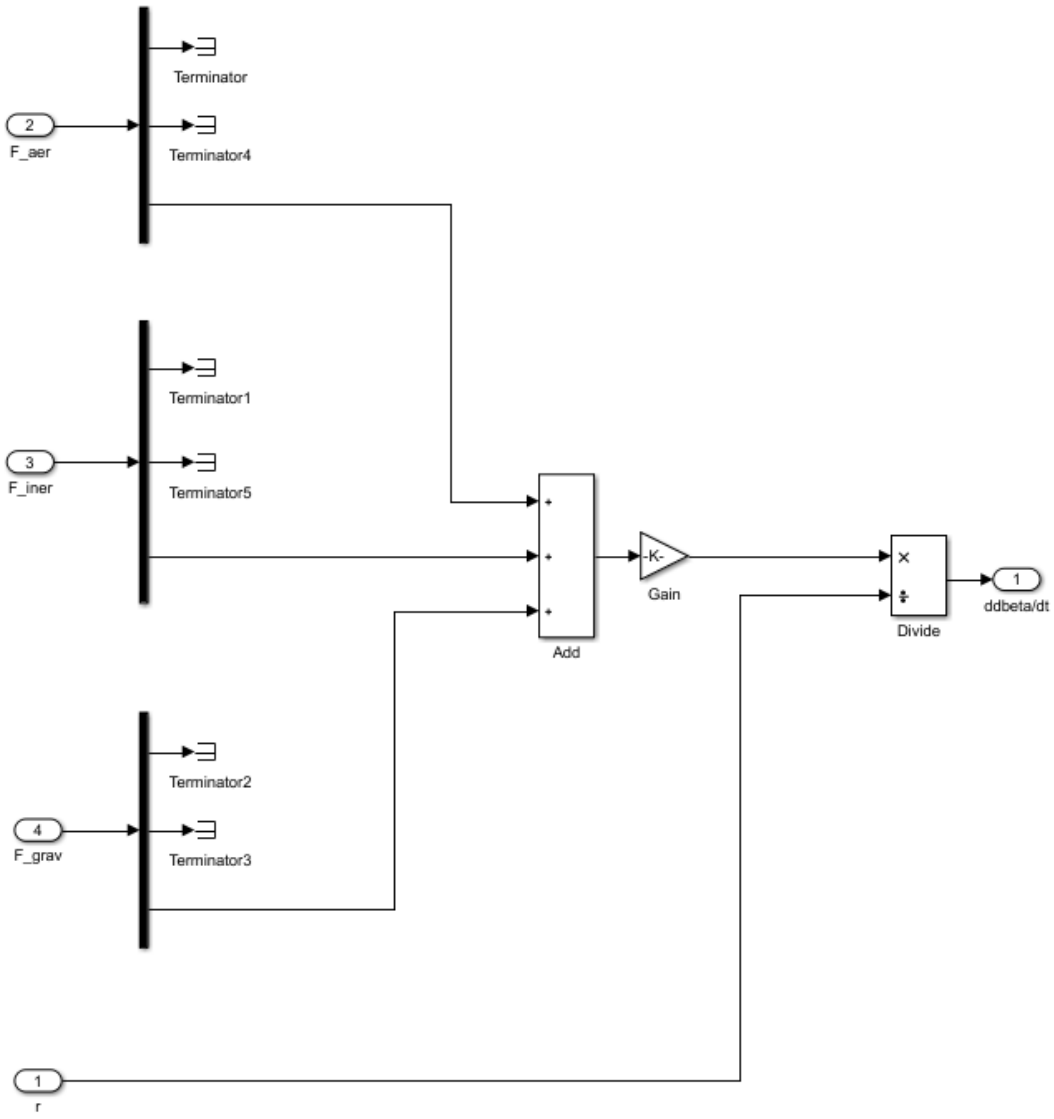

Figure B.8: $\ddot{\beta}$ Subsystem.

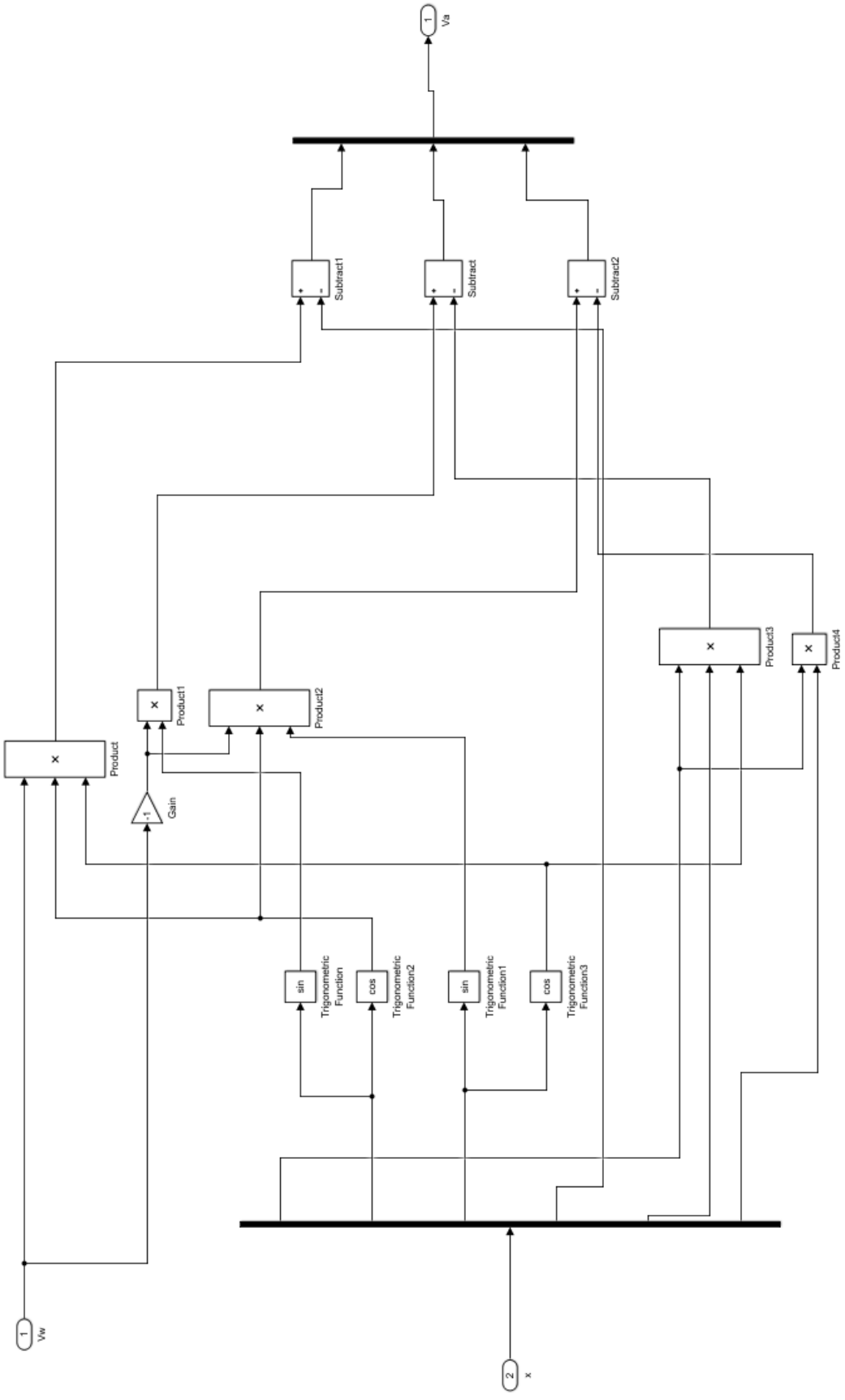

Figure B.9: Wind Apparent Velocity Subsystem.

Bibliography

[1] F. A. Fontes and L. T. Paiva, "UP WIND Project," 2017.

[2] M. C. Fernandes, G. B. Silva, L. T. Paiva, and F. A. Fontes, "A Trajectory Controller for Kite Power Systems with Wind Gust Handling Capabilities," in *Proceedings of 15th International Conference on Informatics in Control, Automation and Robotics (ICINCO)*, (Porto), 2018.

[3] B. Kahn, "We Just Breached the 410 Parts Per Million Threshold," Apr. 2017.

[4] "Europe 2020 Strategy."

[5] "Renewables 2017," tech. rep., International Energy Agency, 2017.

[6] GWEC, "Global Wind Report," tech. rep., 2017.

[7] R. Thresher, M. Robinson, and P. Veers, "To Capture the Wind," *IEEE Power & Energy Magazine*, 2007.

[8] A. Cherubini, *Advances in Airborne Wind Energy and Wind Drones*. PhD, Scuola Superiore Sant'Anna, Pisa, Italy, 2017.

[9] M. L. Loyd, "Crosswind kite power," *Journal of Energy*, vol. 4, no. 3, pp. 106–111, 1980.

[10] T. Sugimoto, "MECHANICS OF CLASSICAL KITE BUGGYING OR how MR. POCOCK GAINED 9 M/S BY HIS CHARVOLANT," (Taipei, Taiwan), 2009.

[11] R. Schmehl, *Airborne Wind Energy: Advances in Technology Development and Research*. Springer, 2018.

[12] e Kite, "e-Kite," 2017.

[13] AmpyxPower, "Ampyx Power," 2017.

[14] "KiteGen."

[15] EnerKíte, "EnerKíte - Airborne Windenergy Converters," 2017.

[16] KitePower, "Kite Power," 2017.

[17] MakaniPower, "Makani | Makani," 2017.

[18] "Altaeros."

[19] "Omnidea | aerial platforms."

[20] R. Schmehl, M. Noom, and R. Van der Vlugt, "Traction Power Generation with Tethered Wings," in *Airborne Wind Energy* (U. Ahrens, M. Diehl, and R. Schmehl, eds.), Green Energy and Technology, Berlin, Heidelberg: Springer Berlin Heidelberg, 2013.

[21] L. T. Paiva and F. A. C. C. Fontes, "Optimal Control Algorithms with Adaptive Time-Mesh Refinement for Kite Power Systems," *Energies*, vol. 11, p. 475, Feb. 2018.

[22] M. Diehl, *Real-time optimization for large scale nonlinear processes*. PhD Thesis, 2001.

[23] L. T. Paiva and F. A. Fontes, "Optimal control of underwater kite power systems," in *Energy and Sustainability in Small Developing Economies (ES2DE), 2017 International Conference in*, pp. 1–6, IEEE, 2017.

[24] "CLARK Y AIRFOIL (clarky-il)."

[25] L. Fagiano, A. U. Zgraggen, M. Morari, and M. Khammash, "Automatic Crosswind Flight of Tethered Wings for Airborne Wind Energy: Modeling, Control Design, and Experimental Results," *IEEE Transactions on Control Systems Technology*, vol. 22, pp. 1433–1447, July 2014.

[26] I. Van der Hoven, "Power Spectrum of Horizontal Wind Speed in the Frequency Range from 0.0007 to 900 Cycles per Hour," *Journal of Meteorology*, vol. 14, 1957.

[27] F. Bianchi, H. Battista, and R. Mantz, "The Wind and Wind Turbines," in *Wind Turbine Control Systems*, 2007.

[28] R. Castro, *Uma Introdução às Energias Renováveis*. IST - Instituto Superior Técnico, 2011.

[29] "Global Wind Atlas."

[30] M. Diehl, "Airborne Wind Energy: Basic Concepts and physical Foundations," in *Airborne Wind Energy*, Springer Berlin Heidelberg, 2013.

[31] I. Argatov and V. Shafranov, "Economic assessment of small-scale kite wind generators," *Renewable Energy*, vol. 89, pp. 125–134, 2016.

[32] "Industrial Catalog," 2010.

[33] J. Heilmann and C. Houle, "Economics of Pumping Kite Generators," in *Airborne Wind Energy* (U. Ahrens, M. Diehl, and R. Schmehl, eds.), Green Energy and Technology, Berlin, Heidelberg: Springer Berlin Heidelberg, 2013.

[34] L. Fagiano and T. Marks, "Design of a Small-Scale Prototype for Research in Airborne Wind Energy," *IEEE/ASME Transactions on Mechatronics*, vol. 20, 2015.

[35] J. Heilmann, "The Technical and Economic Potential of Airborne Wind Energy," Master's thesis, Utrecht University, Utrecht, 2012.

[36] EWEA, "Wind Energy - The Facts," tech. rep., European Wind Energy Association, 2009.

[37] L. Fagiano, M. Milanese, and D. Piga, "High-Altitude Wind Power Generation," *IEEE TRANSACTIONS ON ENERGY CONVERSION*, vol. 25, 2010.

[38] M. Canale, L. Fagiano, and M. Milanese, "High Altitude Wind Energy Generation Using Controlled Power Kites," *IEEE TRANSACTIONS ON CONTROL SYSTEMS TECHNOLOGY*, vol. 18, 2010.

[39] "Study on Challenges in the commercialisation of airborne wind energy systems," tech. rep., European Commission, Directorate-General for Research & Innovation Draft Final Report, Rotterdam, June 2018.

[40] P. Faggiani, "Pumping Kites Wind Farm," Master's thesis, TU Delft, Netherlands, 2014.